

## Article

# Energy Dissipation and Fracture Mechanism of Layered Sandstones under Coupled Hydro-Mechanical Unloading

Zhixiang Song , Junwen Zhang \*  and Shaokang Wu

School of Energy and Mining Engineering, China University of Mining and Technology (Beijing), Beijing 100083, China; szxcumtb@126.com (Z.S.); wsk13037896248@126.com (S.W.)

\* Correspondence: zhangjw@cumtb.edu.cn; Tel.: +86-13681359725

**Abstract:** Rock burst is easy to occur in the water-rich roadway of coal mines, which is closely related to the energy dissipation and fracture mechanism of rocks under coupled hydro-mechanical (H-M) unloading. Therefore, in combination with the triaxial loading and unloading process and H-M coupling effect, the mechanical test of layered sandstones under coupled hydro-mechanical unloading (TLUTP) was conducted. The energy dissipation and fracture mechanism were revealed. The results show that: (1) The influence of layered angles on the peak volumetric strain is more sensitive than that of confining pressure under conventional triaxial loading with H-M coupling (CTLTP). On the contrary, the influence of confining pressure on the peak volumetric strain is more sensitive than that of layered angles under TLUTP. (2) With increasing layered angles, the peak elastic energy density under CTLTP shows the “W” shaped evolution characteristic, while that of under TLUTP shows the “N” shaped evolution characteristic. (3) The “Energy Flow” chain is proposed. Meanwhile, combined with the domino effect and the structural evolution theory, the energy dissipation and fracture mechanism of layered sandstones under coupled hydro-mechanical unloading are both revealed. The conclusions obtained can provide certain fundamental theoretical references for the effective prevention of rock burst in a layered water-rich roadway.

**Keywords:** coupled hydro-mechanical unloading; energy evolution; fracture mechanism; “Energy Flow” chain; rock burst



**Citation:** Song, Z.; Zhang, J.; Wu, S.

Energy Dissipation and Fracture Mechanism of Layered Sandstones under Coupled Hydro-Mechanical Unloading. *Processes* **2023**, *11*, 2041. <https://doi.org/10.3390/pr11072041>

Academic Editor: Qingbang Meng

Received: 20 June 2023

Revised: 3 July 2023

Accepted: 5 July 2023

Published: 7 July 2023



**Copyright:** © 2023 by the authors. Licensee MDPI, Basel, Switzerland. This article is an open access article distributed under the terms and conditions of the Creative Commons Attribution (CC BY) license (<https://creativecommons.org/licenses/by/4.0/>).

## 1. Introduction

The energy dissipation and fracture mechanism of rocks under coupled hydro-mechanical unloading is not only one of the research hotspots in geotechnical engineering, but is also one of the key scientific issues to be solved in deep engineering [1–3]. In addition, related results showed that rock burst is easy to occur in the water-rich roadway of coal mines, which is closely related to the energy dissipation and fracture mechanism of rocks under coupled hydro-mechanical unloading [4–6].

Generally, the joints of rocks develop actively, which show significant anisotropy [7,8]. Meanwhile, sandstone, as one of the geological rocks, is common in numerous large-scale engineering [9–11]. Further, there are the evolution characteristics of in situ stress on the surrounding rocks of layered water-rich roadways before, in and after excavation in Figure 1 [12,13]. Among them, the surrounding rocks of layered water-rich roadways before excavation are subjected to the long-term comprehensive actions of high geo-stress and strong osmotic pressure, which result in the high-density compaction of layered rock strata, and are accompanied by accumulated energy (see Figure 1a). The surrounding rocks of layered water-rich roadways during excavation are in the unloading state of horizontal principal stress, and the accumulated energy is released (see Figure 1b). However, the surrounding rocks of layered water-rich roadways after excavation are subjected to the long-term superimposed actions of the self-weight of the overlying strata (vertical stress) and the mining stress. Subsequently, it easily leads to energy accumulation, and the occurrence of a

series of mechanical behaviors such as large deformation or collapsed failure, and even the occurrence of rock burst (see Figure 1c). Therefore, the energy dissipation law and fracture mechanism of layered sandstones under coupled hydro-mechanical unloading needed to be further studied.

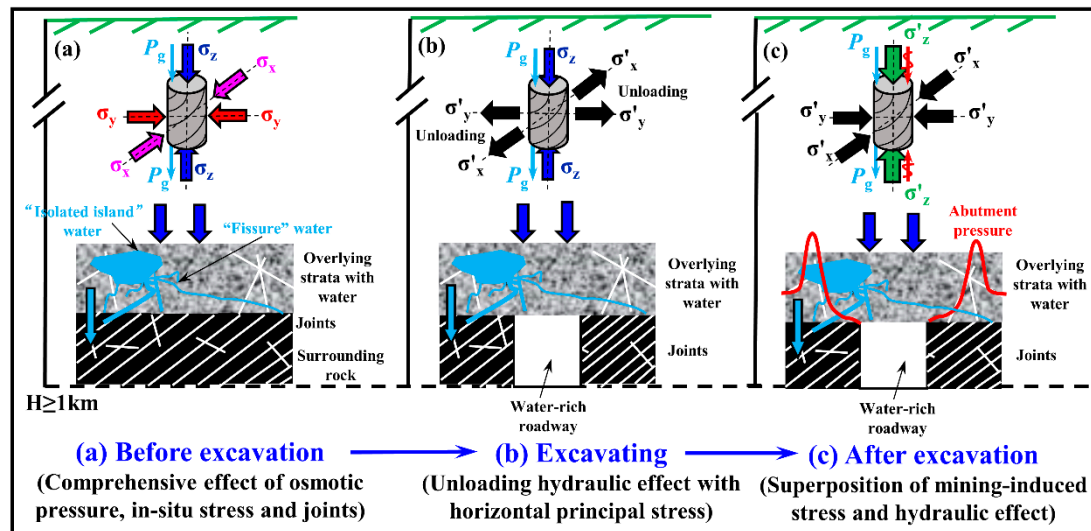


**Figure 1.** Geo-stress distribution characteristic of deep surrounding rocks in a layered water-rich roadway.

Currently, related research on the energy dissipation law and fracture mechanism of rocks has been conducted by numerous researchers, and relatively abundant results have been obtained. Among them, the energy dissipation law of coal or rocks under a single stress field have both been studied. Subsequently, the energy dissipation law and fracture mechanism of rocks under the single stress field was better revealed [14–26]. In addition, Professor Gong's team has conducted numerous laboratory mechanical experiments on rocks, where the linear energy evolution law and the fracture mechanism of rocks were further found and revealed [27–31]. Meanwhile, numerous researchers have constructed a series of damage evolution models and failure criterions of coal or rocks. For example, the damage constitutive models of brittle rocks according to the energy dissipation law and fracture mechanism were constructed [32–34]. Moreover, a series of failure criterions of rocks under different loading modes were also constructed [35–38].

Furthermore, the creep mechanical behavior and time-dependent initiation, propagation and interaction mechanism of rock-like mortar with three-dimensional cracks under triaxial H-M coupling were deeply studied [39,40]. Subsequently, it was concluded that sub-critical crack propagation is the main failure cause of rocks, and the faster the propagation rate of dominant cracks, the more severe the failure rate of rocks. Moreover, the mechanical behaviors of single-fissure mudstone under triaxial compression shear with H-M coupling have been analyzed. Subsequently, it was concluded that the single-fissure mudstone was most prone to failure when the fissure angle was 45° [41]. Additionally, the mechanical behavior of jointed rocks under H-M coupling was characterized, and its damage constitutive model was constructed [42]. Moreover, a micromechanical hydro-mechanical-damage coupling model was established based on consideration of the multi-scale structural differences of layered rocks [43]. In addition, the evolution law of the permeability coefficient and fracture mechanism of rocks under various confining pressures was characterized and revealed, respectively [44]. The corresponding hydro-mechanical-damage coupling evolution model according to the damage evolution characteristics of the plastic dilatation of anisotropic rocks under H-M coupling have been also established [45,46].

This brief literature survey shows that the focus has mainly been on the energy dissipation law and fracture mechanism of rocks under a single stress field. However, there are

relatively rare reports of coupled hydro-mechanical unloading. Therefore, the corresponding coupled hydro-mechanical unloading experimentation of layered sandstones has been conducted. Firstly, the anisotropy and competition relationship of energy are obtained. Secondly, the corresponding energy evolution model is established. Meanwhile, the energy evolution and failure mechanism are revealed. Subsequently, the occurrence mechanism of rock burst in a layered water-rich roadway is revealed according to the proposed theory of an “Energy Flow” chain. Meanwhile, the specific discriminant formula with the form of “Energy Flow” of rock burst in a layered water-rich roadway is qualitatively proposed. Finally, the nature of the effective prevention and accurate control of rock burst is obtained from three aspects, which corresponded to that controlling the starting source, cutting off the “Energy Flow” chain, and protecting the target source.

## 2. Preparation and Test Plans

A series of processing works were conducted on the large, layered sandstones taken from the sampling site, including drilling, cutting and polishing. Subsequently, the standard specimens were obtained.

The TOP INDUSTRIE Rock 600-50 multi-field coupling test system was used for the mechanical tests under H-M coupling. Among them, the stress paths adopted could be seen in Figure 2. The corresponding test plans were as follows:

### 1. Conventional triaxial loading test under H-M coupling (CTLTP)

(a) Stage I: Confining pressure loading stage. At this stage, the confining pressure  $\sigma_3$  was loaded to the corresponding pre-set value  $a$  ( $a = 10, 20, 30$  MPa) by the hydrostatic pressure, respectively. Meanwhile, the loading rate adopted at this stage was 1 MPa/min.

(b) Stage ①: Osmotic pressure loading stage. At this stage, the axial pressure  $\sigma_1$  and confining pressure  $\sigma_3$  were kept constant. Then, the osmotic pressure  $P_g$  was loaded to the corresponding pre-set value of 4 MPa with the stress-controlled mode. Meanwhile, the loading rate adopted at this stage was 1 MPa/min.

(c) Stage II: Axial stress loading stage. At this stage, the osmotic pressure  $P_g$  and confining pressure  $\sigma_3$  were kept constant. Then, the axial pressure  $\sigma_1$  was loaded until failure in terms of the strain-controlled mode. Meanwhile, the loading rate adopted at this stage was 0.06 mm/min.

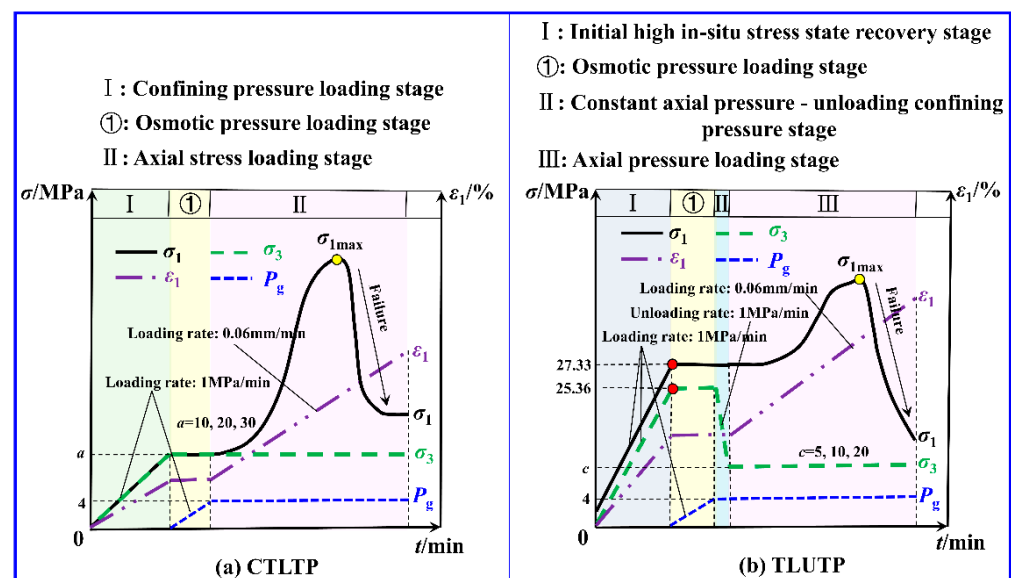


Figure 2. Triaxial loading (unloading) stress paths under H-M coupling: (a) CTLTP, (b) TLUTP.

## 2. Triaxial loading and unloading test under H-M coupling (TLUTP)

(a) Stage I: Initial high in situ state recovery stage. At this stage, the confining pressure  $\sigma_3$  and axial pressure  $\sigma_1$  were loaded to the  $\sigma_1 = 27.33$  MPa,  $\sigma_3 = 25.36$  MPa (corresponding to the buried depth of the sampling site) by the deviatoric stress. Meanwhile, the loading rate adopted at this stage was 1 MPa/min.

(b) Stage ①: Osmotic pressure loading stage. At this stage, the  $\sigma_1 = 27.33$  MPa,  $\sigma_3 = 25.36$  MPa was kept constant. The osmotic pressure  $P_g$  was loaded to the corresponding pre-set value of 4 MPa in terms of the stress-controlled mode. Meanwhile, the loading rate adopted at this stage was 1 MPa/min.

(c) Stage II: Constant axial pressure–unloading confining pressure stage. At this stage, the osmotic pressure  $P_g$  and axial pressure  $\sigma_1$  were kept constant. Then, the confining pressure  $\sigma_3$  was unloaded to the corresponding pre-set value  $c$  ( $c = 5, 10, 20$  MPa) in terms of the stress-controlled mode. Meanwhile, the unloading rate adopted at this stage was 1 MPa/min.

(d) Stage III: Axial stress loading stage. At this stage, the osmotic pressure  $P_g$  and confining pressure  $\sigma_3$  were kept constant. Then, the axial pressure  $\sigma_1$  was loaded until failure in terms of the strain-controlled mode. Meanwhile, the loading rate adopted at this stage was 0.06 mm/min.

## 3. Results

### 3.1. Stress–Strain Behavior and Fracture Modes

As shown in Figures 3 and 4, the global radial deformation of layered sandstones under TLUTP was significantly weaker than that under CTLTP. In addition, the global axial deformation with CTLTP under an identical layered angle and various confining pressures had little differences. However, the global axial deformation with CTLTP under identical confining pressure and various layered angles was quite different. Therefore, the influence of confining pressure was not sensitive to the global axial deformation under CTLTP. However, the bedding effect was sensitive to the global axial deformation under CTLTP.

Nevertheless, the effects of confining pressure and bedding were both sensitive to the global axial deformation under TLUTP. It was also indicated that there were certain errors in estimating the deformation resistance of deep surrounding rocks only according to the results of CTLTP. Therefore, the stress path of TLUTP should be vigorously adopted to conduct a series of related research. Thus, it was expected that the deformation resistance of deep surrounding rocks could be estimated more accurately.

In addition, the peak strength with TLUTP was higher than that with CTLTP under identical working conditions. Therefore, to more accurately estimate the bearing capacity and deformation resistance of deep surrounding rocks, it was necessary to fully rely on the stress path of TLUTP to conduct the laboratory mechanical research.

In addition, as shown in Figures 3–5, layered sandstones under CTLTP and TLUTP showed four types of macroscopic fracture modes. Among them, the macroscopic fracture mode with layered angles of  $0^\circ$ ,  $30^\circ$  and  $90^\circ$  basically belonged to type III. However, the macroscopic fracture mode with a  $45^\circ$  layered angle belonged to type II. Meanwhile, the macroscopic fracture mode with a layered angle of  $60^\circ$  basically belonged to type I. Among them, the comprehensive effects of stress path CTLTP, bedding angle  $0^\circ$  and confining pressure 20 MPa led to the macroscopic fracture mode belonging to type IV. It was suggested that the influences of the stress path and confining pressure had little effects on the macroscopic fracture mode, but the bedding effect had significant influences on the macroscopic fracture mode.

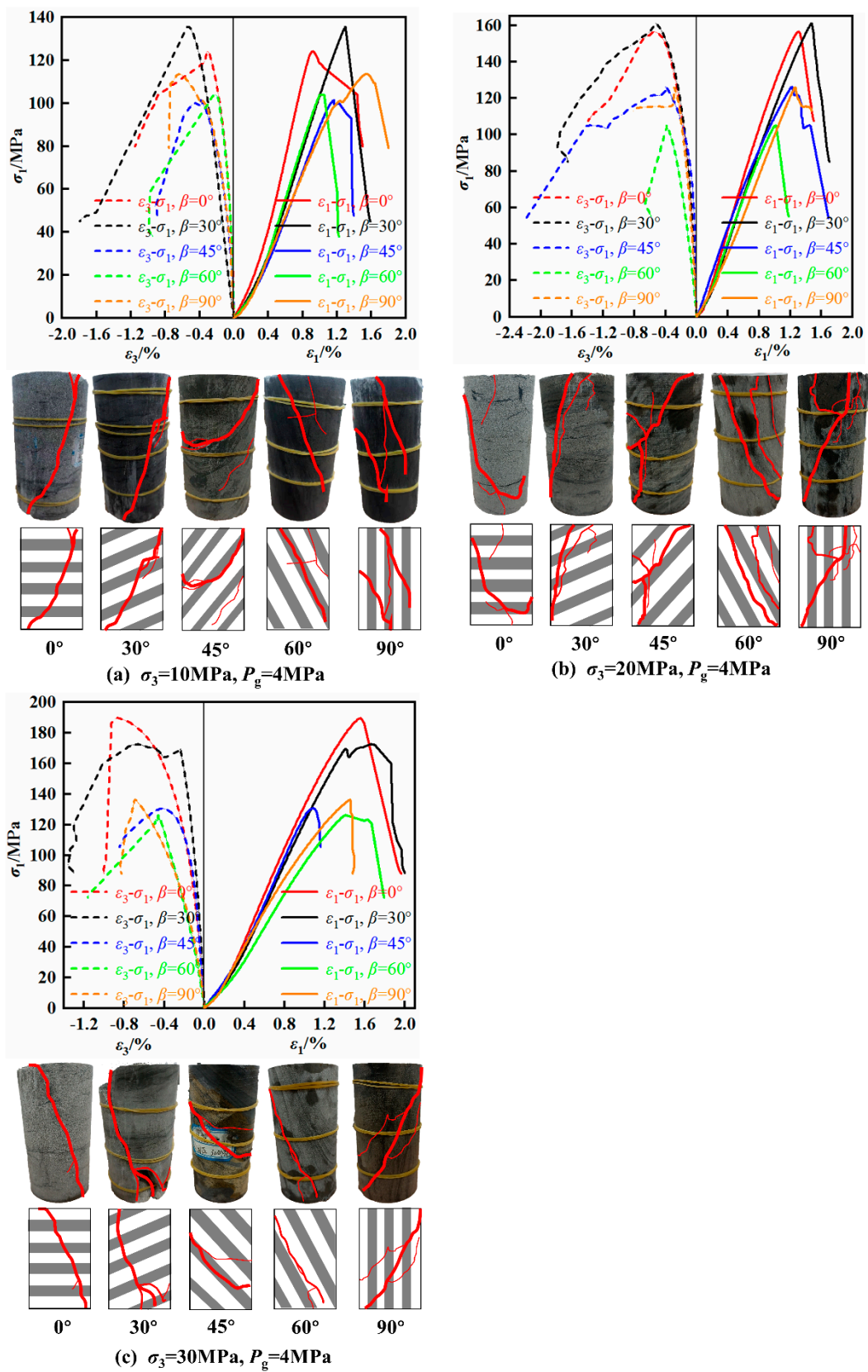


Figure 3. Stress–strain behavior and fracture model under CTLTP.

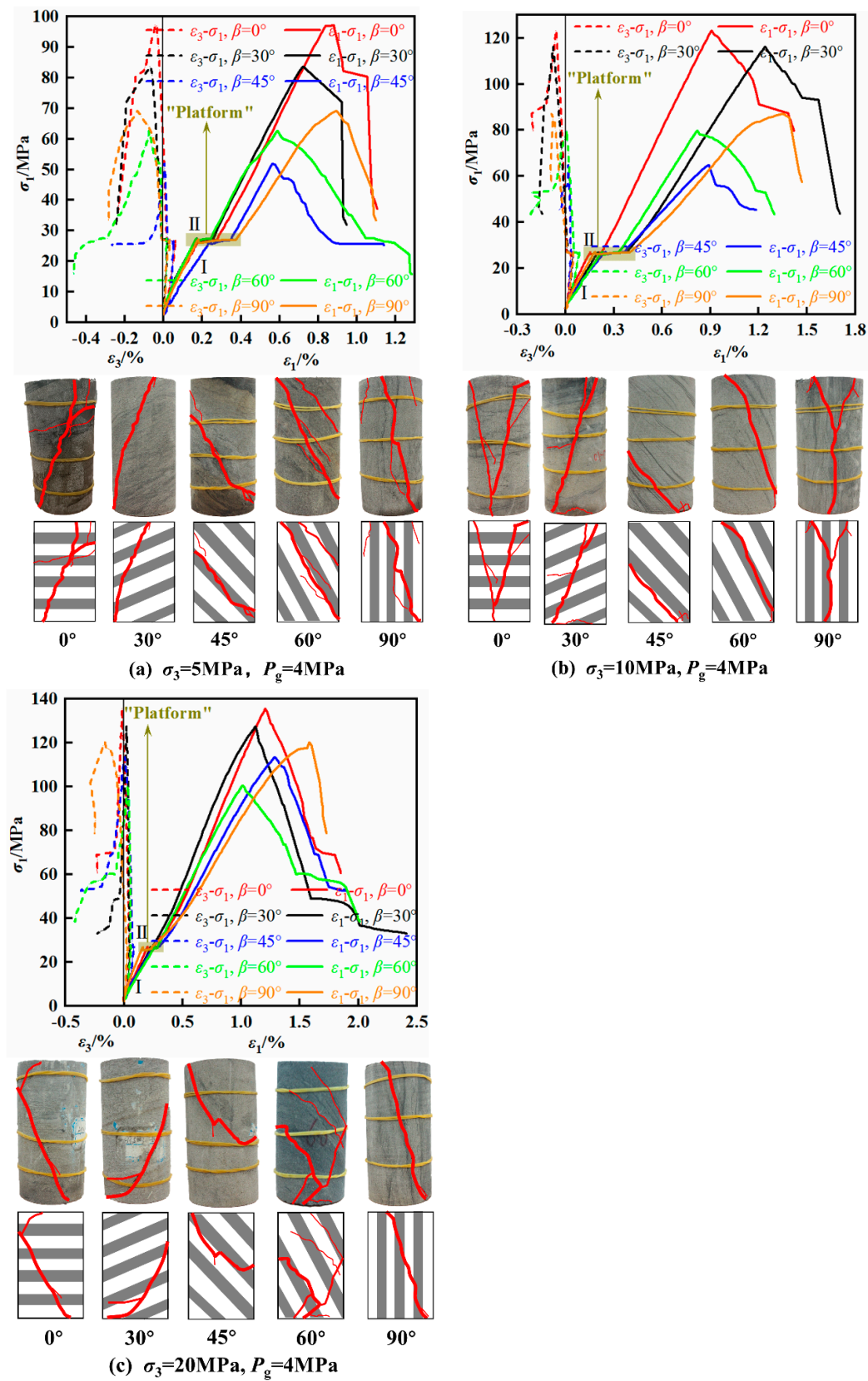


Figure 4. Stress–strain behavior and fracture model under TLUTP.

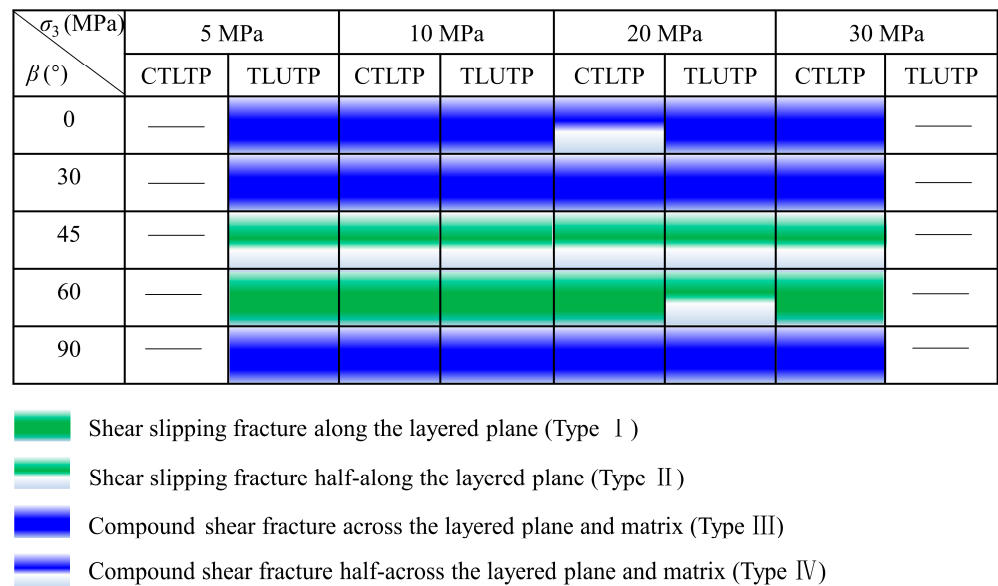


Figure 5. Macroscopic fracture modes.

In addition, the fracture modes under CTLTP and TLUTP were mainly shear fracture, which suggested that there must be a weak structure with the lowest bearing capacity in layered sandstones [47,48]. Under the actions of the effective triaxial loads, the weak structure could gradually develop and finally formed the shear fracture dominated by single- or crossing-fracture planes.

### 3.2. Strength Anisotropy and Deformation Evolution

There were significant influences of confining pressure on the peak strength under CTLTP and TLUTP (see Figure 6). Meanwhile, with the increase of confining pressure, the peak strength under CTLTP and TLUTP was raised. However, when  $\beta \in (0^\circ, 30^\circ)$  and  $\beta \in (45^\circ, 90^\circ)$ , the peak strength under an identical confining pressure changed little, which suggested that the influenced sensitivity of the layered angles compared to that of the confining pressure on the peak strength under TLUTP was weaker. However, when  $\beta \in (30^\circ, 45^\circ)$ , the influence of the layered angles on the peak strength was more sensitive than that of confining pressure.

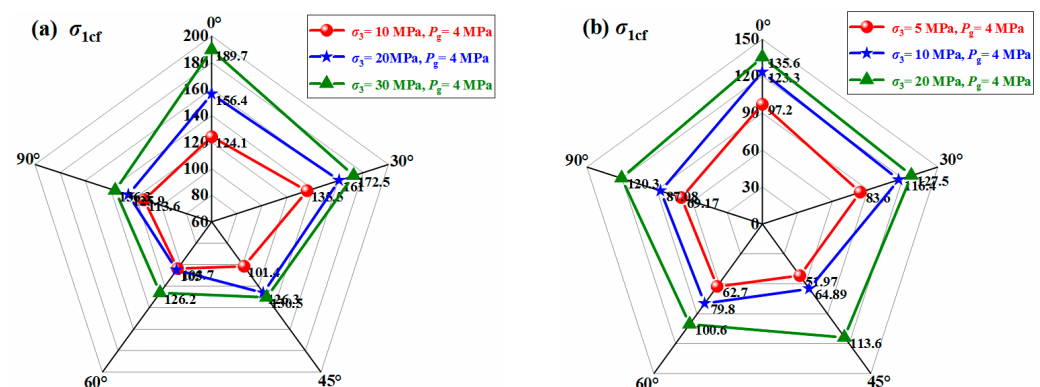


Figure 6. Peak strength: (a) CTLTP, (b) TLUTP.

The peak axial strain with CTLTP was generally higher than that with TLUTP under identical working conditions (see Figure 7). Corresponding to the deep excavation engineering, there were errors in the estimating results for the deformation resistance of deep surrounding rocks in terms of the stress path CTLTP. Therefore, it is necessary to conduct a series of related studies adopting the stress path TLUTP to more accurately estimate the deformation resistance of deep surrounding rocks. In addition, the influence of confining pressure on the peak axial strain was more significant than that of layered angles.

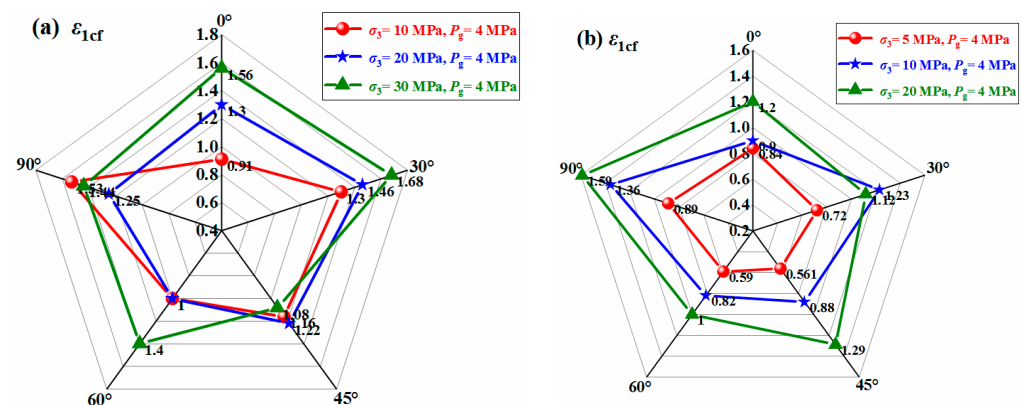


Figure 7. Peak axial strain: (a) CTLTP, (b) TLUTP.

As shown in Figure 8, compared with TLUTP, CTLTP had the more significant influence on the peak radial strain, and the anisotropy of peak radial strain under CTLTP was more significant. In addition, the influenced sensitivity of confining pressure on the peak radial strain under CTLTP was significantly stronger than that of layered angles. However, the anisotropy of peak radial strain with TLUTP under low confining pressure was significant.

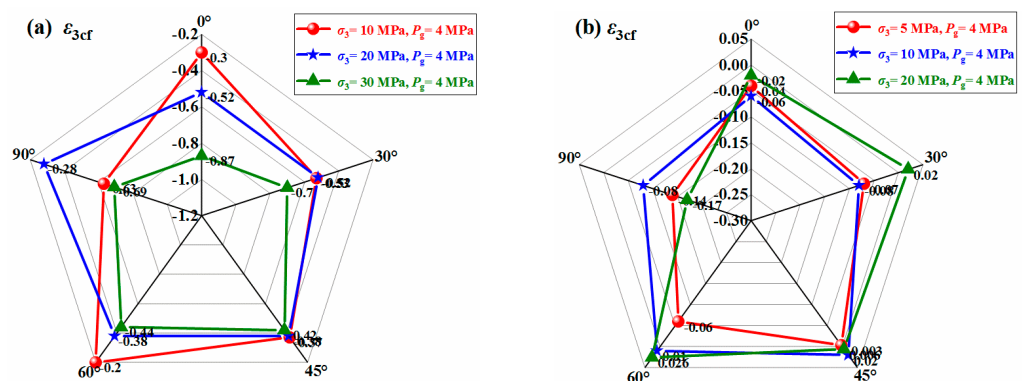


Figure 8. Peak radial strain: (a) CTLTP, (b) TLUTP.

The influence of confining pressure on the peak volumetric strain under TLUTP was also significant (see Figure 9). Due to the comprehensive actions of the layered angles, stress path, confining pressure and osmotic pressure, the evolution characteristics of peak volumetric strain under CTLTP were significantly different. In addition, the influences of layered angles were more sensitive on the peak volumetric strain under CTLTP than that of confining pressure. Nevertheless, the influence of confining pressure on the peak volumetric strain under TLUTP was more sensitive than that of layered angles.

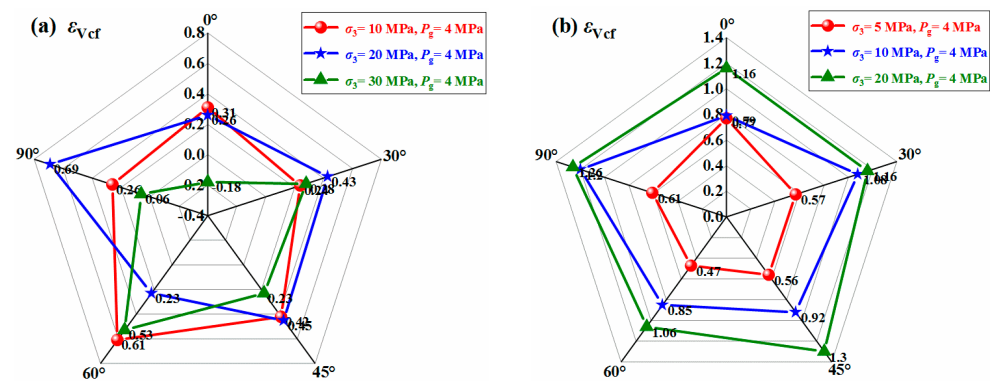


Figure 9. Peak volumetric strain: (a) CTLTP (b) TLUTP.

### 3.3. Energy Evolution

Under the comprehensive actions of loading or unloading, the energy evolution under H-M coupling still follows the first thermodynamics law [49], namely

$$U_t^P = U_e^P + U_d^P \quad (1)$$

where  $U_t^P$ ,  $U_e^P$  and  $U_d^P$ , respectively, represent the total input energy density, elastic energy density and dissipated energy density under H-M coupling.

In addition, according to Terzaghi's effective stress principle [50], the effective axial stress  $\sigma'_1$  and the effective confining pressure  $\sigma'_3$  can be expressed as:

$$\begin{cases} \sigma'_1 = \sigma_1 - P_g \\ \sigma'_3 = \sigma_3 - P_g \end{cases} \quad (2)$$

where  $\sigma_1$ ,  $\sigma_3$  and  $P_g$  represent the axial stress, confining pressure and osmotic pressure, respectively.

Meanwhile, combined with Figures 3 and 4 and Equation (2), the total input energy density under H-M coupling can be quantitatively calculated:

$$U_t^P = \int_0^{\varepsilon_{1f}} \sigma'_1 d\varepsilon_1 + 2 \int_0^{\varepsilon_{3f}} \sigma'_3 d\varepsilon_3 \quad (3)$$

In addition, similarly with the calculation method of the elastic energy density under the single stress field, the elastic energy density under H-M coupling can be obtained, and the specific expression is as follows:

$$U_e^P = \frac{1}{2E} [\sigma_1'^2 + 2\sigma_3'^2 - 2\mu(2\sigma_1'\sigma_3' + \sigma_3'^2)] \quad (4)$$

Combining with Equations (1)–(4), the dissipated energy density under H-M coupling can be obtained, and the specific expression is as follows:

$$U_d^P = \int_0^{\varepsilon_{1f}} \sigma'_1 d\varepsilon_1 + 2 \int_0^{\varepsilon_{3f}} \sigma'_3 d\varepsilon_3 - \frac{1}{2E} [\sigma_1'^2 + 2\sigma_3'^2 - 2\mu(2\sigma_1'\sigma_3' + \sigma_3'^2)] \quad (5)$$

where  $E$  represents the elastic modulus, and  $\mu$  represents the Poisson's ratio.  $\varepsilon_{1f}$  and  $\varepsilon_{3f}$  are the final data points of axial strain and radial strain collected by hydraulic coupling tests, respectively.

Therefore, the energy evolution curves under CTLTP and TLUTP are drawn in Figures 10 and 11.

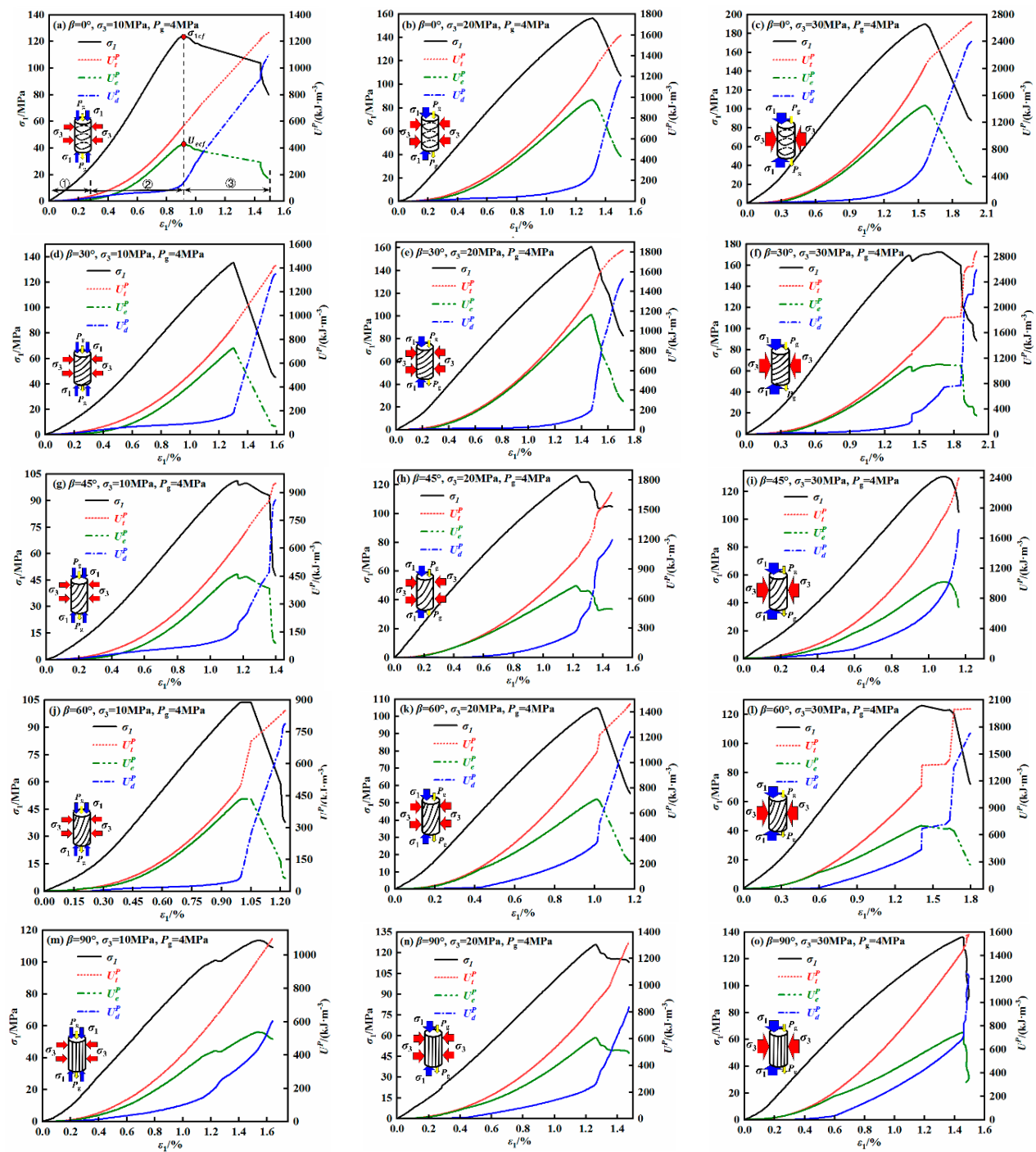


**Figure 10.** Energy evolution under CTLTP.

In addition, the deformation of rocks under identical stress paths has a certain “memory effect”. Naturally, the energy evolution of rocks also has certain similarities. Therefore, the energy evolution curve with CTLTP under a layered angle of  $0^\circ$ , confining pressure of 10 MPa and osmotic pressure of 4 MPa was adopted for representative analysis (see Figure 10a). Similarly, the energy evolution curve with TLUTP under the layered angle of  $0^\circ$ , confining pressure of 5 MPa and osmotic pressure of 4 MPa was adopted for representative analysis (see Figure 11a).

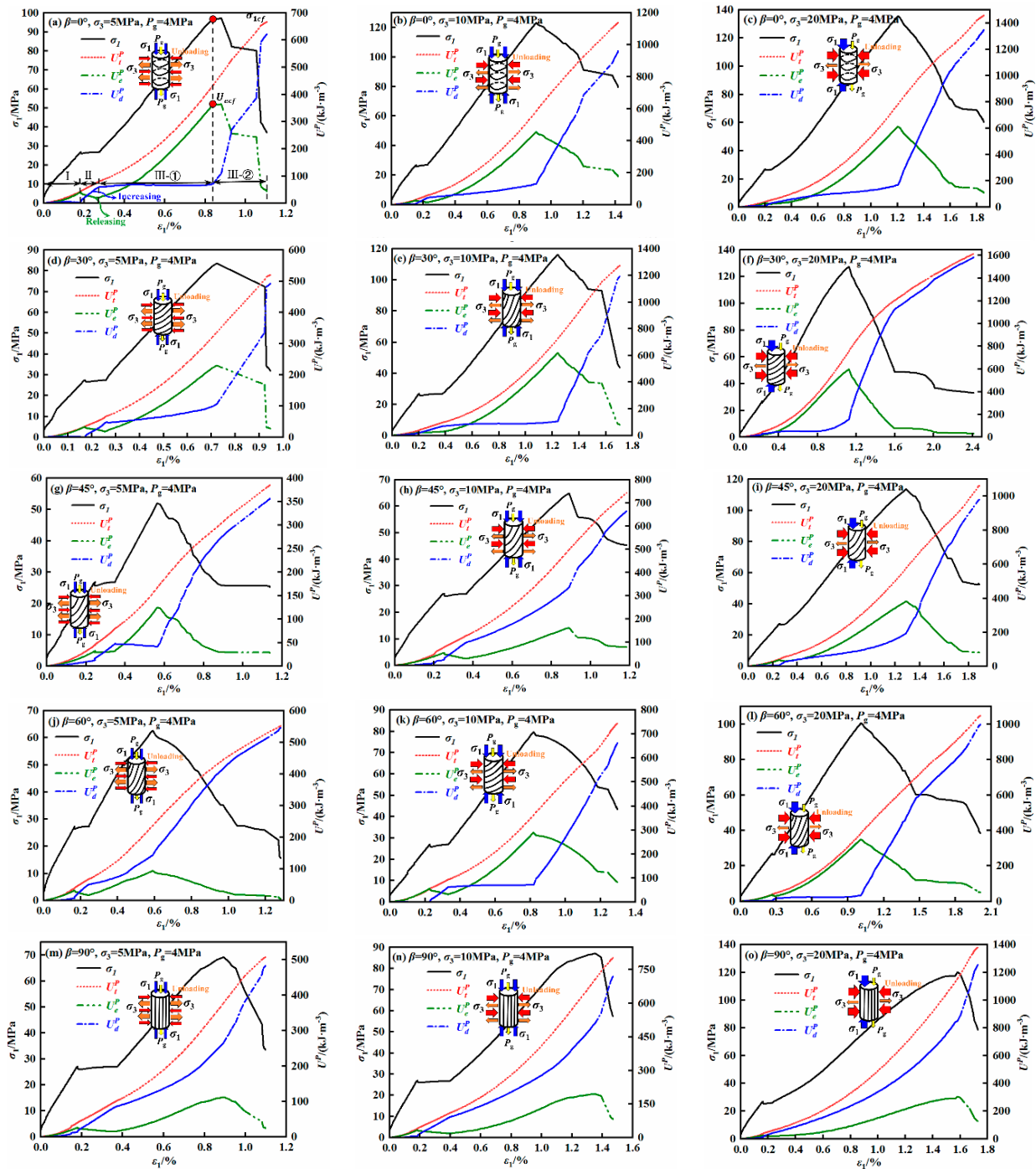


Figure 11. Energy evolution under TLUTP.

As shown in Figures 11a and 12a, the energy evolution under CTLTP could be divided into three stages, while that under TLUTP could be divided into four stages.

Stage ① corresponded to the initial pore compaction stage (see Figure 10a). According to Terzaghi's effective stress principle, the effective stresses at this stage were both small. Therefore,  $U_t^p$ ,  $U_e^p$  and  $U_d^p$  were all seen in the initial incubation stage with small values which, respectively, slowly and synchronously raised ( $0 \rightarrow 4.52 \text{ kJ} \cdot \text{m}^{-3}$ ,  $0 \rightarrow 2.77 \text{ kJ} \cdot \text{m}^{-3}$  and  $0 \rightarrow 1.75 \text{ kJ} \cdot \text{m}^{-3}$ ). Stage I corresponded to the initial high in situ stress state recovery stage (see Figure 11a). At this stage,  $U_t^p$  and  $U_e^p$  raised quickly ( $0 \rightarrow 42.25 \text{ kJ} \cdot \text{m}^{-3}$  and  $0 \rightarrow 38.61 \text{ kJ} \cdot \text{m}^{-3}$ ), while  $U_d^p$  raised in a shapely manner ( $0 \rightarrow 3.64 \text{ kJ} \cdot \text{m}^{-3}$ ). According to Terzaghi's effective stress principle, the existence of high effective confining pressure and

high effective axial pressure made the compaction effect of the three-dimensional volume significantly enhanced at this stage. It could greatly improve the compaction degree of its internal pores and space, and even made it become rigid. The occurrence of this process would inevitably lead to significant elastic energy accumulation, and then cause  $U_t^P$  to increase rapidly. However, at this stage,  $U_d^P$  had almost no change, which was close to the rigid body.

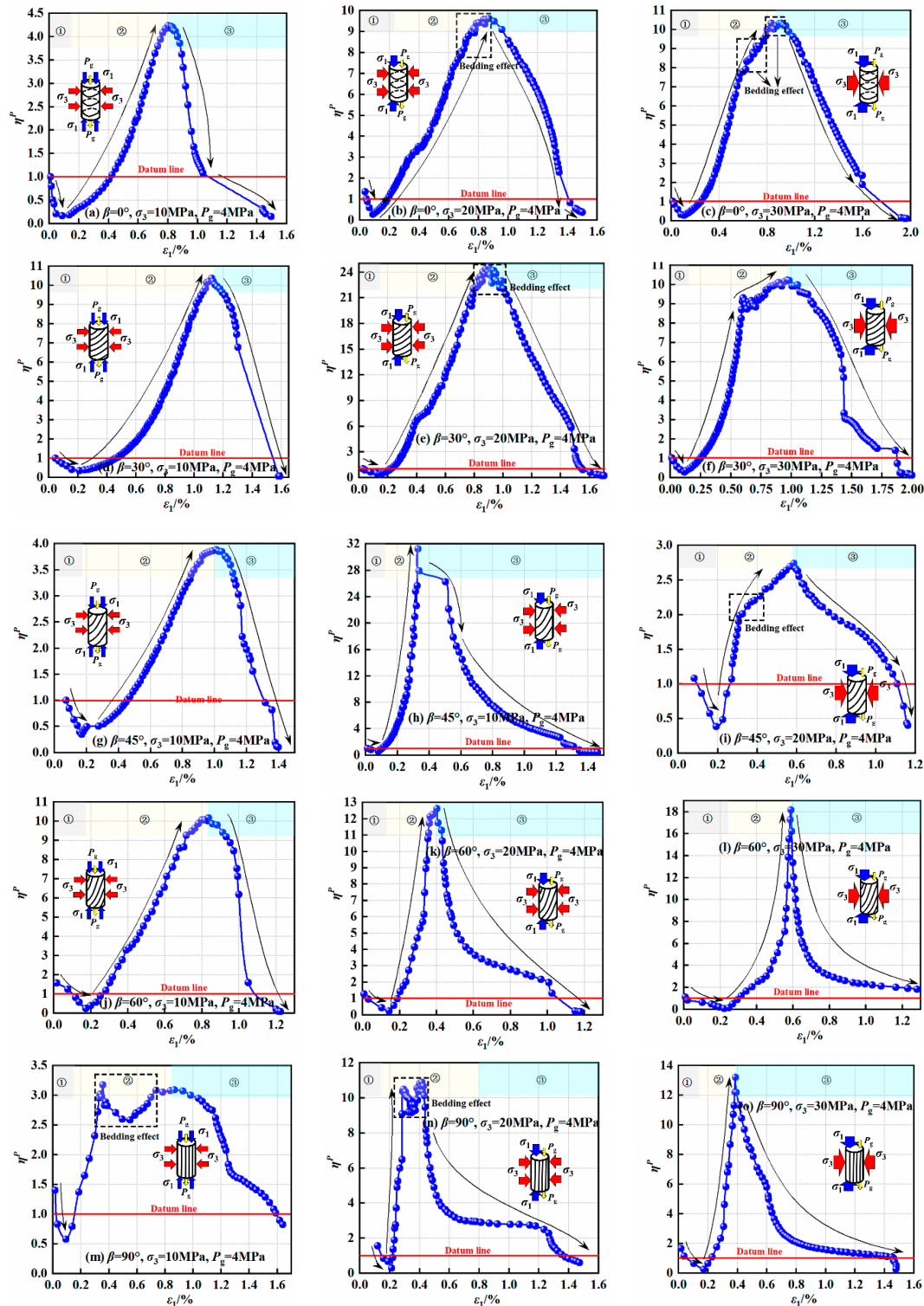


Figure 12. The ratio of elastic energy to dissipated energy under CTLTP.

In Figure 10a, stage ② corresponded to the pre-peak elastic and plastic deformation stage. At this stage, numerous newly formed micro-cracks would gradually derive, develop, nucleate and even coalesce under the actions of external loads, and gradually formed the dominant seepage channels. According to Griffith strength theory [51], numerous newly developed micro-crack tips were easy to form the high-stress concentration zone, which was accompanied by significant energy accumulation. Therefore,  $U_e^P$  raised rapidly ( $2.77 \text{ kJ}\cdot\text{m}^{-3} \rightarrow 42.69 \text{ kJ}\cdot\text{m}^{-3}$ ). Meanwhile, the gradual formation of the dominant seepage channels would cause the seepage water to absorb the energy, and indirectly replaced the position of dissipated energy. Then, it resulted in  $U_d^P$  having almost no change at this stage, which steadily and slowly raised ( $1.75 \text{ kJ}\cdot\text{m}^{-3} \rightarrow 10.49 \text{ kJ}\cdot\text{m}^{-3}$ ). Therefore,  $U_t^P$  raised rapidly ( $4.52 \text{ kJ}\cdot\text{m}^{-3} \rightarrow 53.18 \text{ kJ}\cdot\text{m}^{-3}$ ). In Figure 11a,  $U_e^P$  at stage II rapidly decreased ( $38.61 \text{ kJ}\cdot\text{m}^{-3} \rightarrow 20.40 \text{ kJ}\cdot\text{m}^{-3}$ ), while  $U_d^P$  raised rapidly at this stage ( $3.64 \text{ kJ}\cdot\text{m}^{-3} \rightarrow 60.46 \text{ kJ}\cdot\text{m}^{-3}$ ). Therefore,  $U_t^P$  raised steadily ( $42.25 \text{ kJ}\cdot\text{m}^{-3} \rightarrow 80.85 \text{ kJ}\cdot\text{m}^{-3}$ ). At this stage, the radial unloading effect would appear to a certain extent, so that the openings of internal original micropores were opened again. Meanwhile, the radial openings of the dominant seepage channels were also opened, which led to  $U_e^P$  to be rapidly released and the rapid accumulation of  $U_d^P$  at this stage.

In addition, in Figure 10a, stage ③ corresponded to the post-peak failure stage. At this stage, under the continuous actions of effective stresses, the layered sandstones accumulated significant damage which would further form the macroscopic shear fracture plane. Meanwhile, the dominant seepage channels would also be completely formed, thus leading to the release of  $U_e^P$ . The numerical results showed that  $U_e^P$  decreased rapidly ( $42.69 \text{ kJ}\cdot\text{m}^{-3} \rightarrow 16.61 \text{ kJ}\cdot\text{m}^{-3}$ ),  $U_d^P$  raised rapidly ( $10.49 \text{ kJ}\cdot\text{m}^{-3} \rightarrow 109.99 \text{ kJ}\cdot\text{m}^{-3}$ ) and  $U_t^P$  raised rapidly ( $53.18 \text{ kJ}\cdot\text{m}^{-3} \rightarrow 126.60 \text{ kJ}\cdot\text{m}^{-3}$ ). However, in Figure 11a, stage III-① under TLUTP was varied from stage ② under CTLTP. This stage included the secondary compaction sub-stage, linear elastic deformation sub-stage and plastic deformation sub-stage. Due to the combined actions of stages I and II, the stress–strain curves of the secondary compaction sub-stage and the plastic deformation sub-stage under CTLUP were not significant, and the axial deformation under CTLUP was smaller than that of the whole deformation. However, the energy evolution of stage III-① was similar to that of stage ② in Figure 10a. At this stage, numerous newly formed micro-cracks would gradually derive, develop, nucleate and even coalesce under the actions of external loads, and gradually formed the dominant seepage channels. According to Griffith strength theory, numerous newly developed micro-crack tips can easily form a high-stress concentration zone, which is accompanied by significant energy accumulation. Therefore,  $U_e^P$  at this stage raised rapidly ( $20.40 \text{ kJ}\cdot\text{m}^{-3} \rightarrow 363.48 \text{ kJ}\cdot\text{m}^{-3}$ ). Meanwhile, the gradual formation of the dominant seepage channels would cause the seepage water to absorb part of the energy, and indirectly replace  $U_d^P$ . The result is that  $U_d^P$  had almost no change at this stage, which steadily and slowly raised ( $60.46 \text{ kJ}\cdot\text{m}^{-3} \rightarrow 70.66 \text{ kJ}\cdot\text{m}^{-3}$ ). Therefore,  $U_t^P$  at this stage raised rapidly ( $80.85 \text{ kJ}\cdot\text{m}^{-3} \rightarrow 434.14 \text{ kJ}\cdot\text{m}^{-3}$ ).

In addition, in Figure 11a, stage III-① was the post-peak failure stage under TLUTP. The energy evolution at this stage under TLUTP was similar to that of stage ③ under CTLTP. At this stage, under the continuous actions of effective stresses, the layered sandstone that accumulated a lot of damage would further form the macroscopic shear fracture plane. Meanwhile, the dominant seepage channels would also be completely formed, thus leading to the release of  $U_e^P$ . The numerical results showed that  $U_e^P$  decreased rapidly ( $363.48 \text{ kJ}\cdot\text{m}^{-3} \rightarrow 44.43 \text{ kJ}\cdot\text{m}^{-3}$ ),  $U_d^P$  raised rapidly ( $70.66 \text{ kJ}\cdot\text{m}^{-3} \rightarrow 623.52 \text{ kJ}\cdot\text{m}^{-3}$ ) and  $U_t^P$  raised rapidly ( $434.14 \text{ kJ}\cdot\text{m}^{-3} \rightarrow 667.95 \text{ kJ}\cdot\text{m}^{-3}$ ).

### 3.4. Energy Competition Relationship

There was a significant energy competition relationship. Therefore, the evolution curve of the ratio of elastic energy density to dissipated energy density  $\eta^P$  under CTLTP and TLUTP with axial strain  $\varepsilon_1$  was drawn (see Figures 12 and 13).

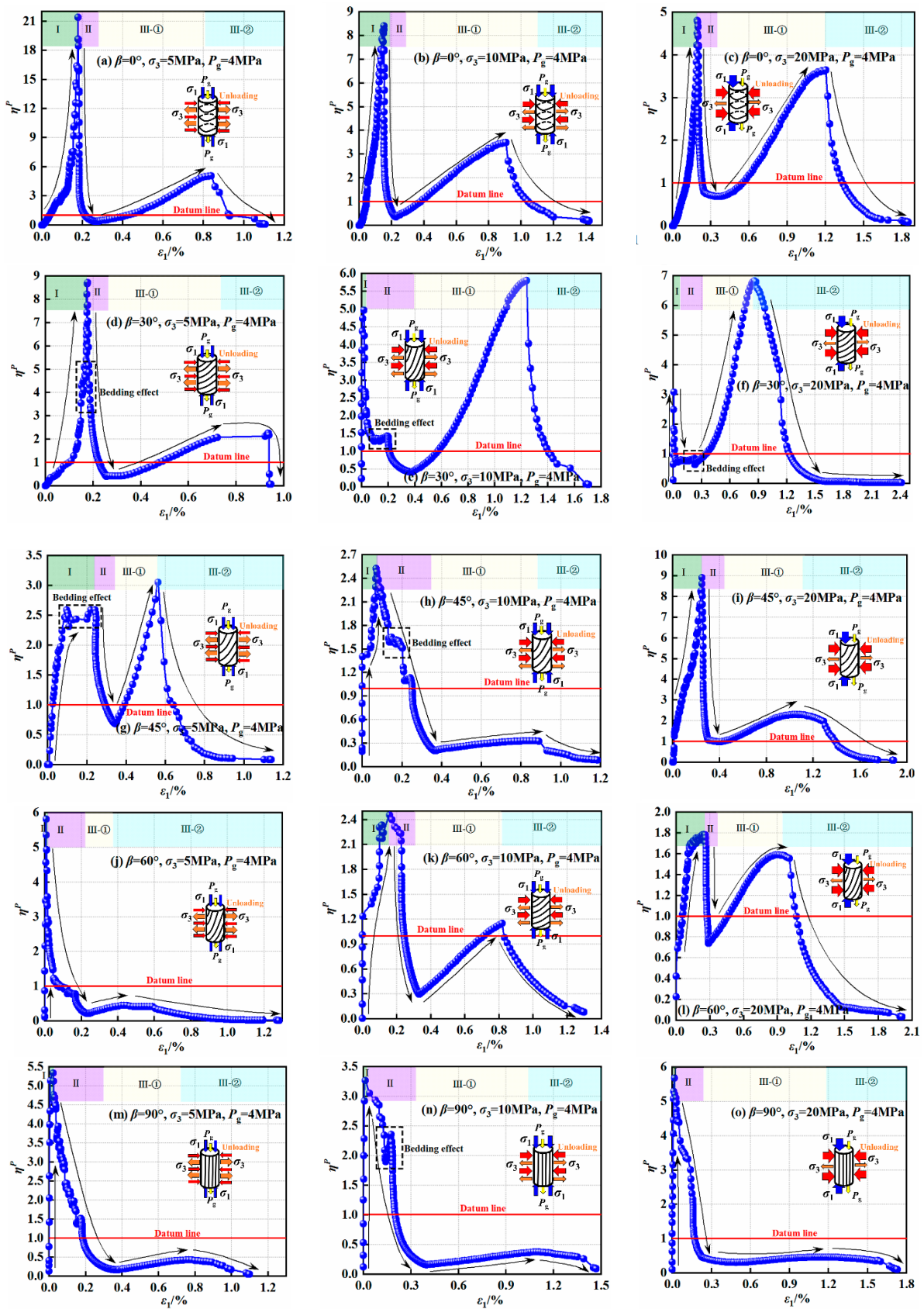


Figure 13. The ratio of elastic energy to dissipated energy under TLUTP.

Similarly, the  $\eta^P$  evolution curve with CTLTP under a layered angle of  $0^\circ$ , confining pressure of 10 MPa and osmotic pressure of 4 MPa was adopted for representative analysis (see Figure 12a). Similarly, the  $\eta^P$  evolution curve with TLUTP under a layered angle of  $0^\circ$ , confining pressure of 5 MPa and osmotic pressure of 4 MPa was adopted for representative analysis (see Figure 13a).

As shown in Figures 12a and 13a, the evolution curves of  $\eta^P$  under CTLTP could be divided into three stages, which showed the inverse “N” type evolution characteristic first decreasing, then increasing and finally decreasing again. However, the evolution curves of  $\eta^P$  under TLUTP could be divided into four stages, which showed the “M” type evolution characteristic first increasing, then decreasing, then increasing again, and finally decreasing again.

Among them, in Figure 12a, stage ① corresponded to the initial pore compaction stage. At this stage,  $\eta^P$  dropped rapidly from 1.01 to 0.159, which indicated that compared with  $U_e^P$ ,  $U_d^P$  at this stage was dominant. It was also suggested that the accumulation rate of  $U_e^P$  at this stage was weaker than the derivation rate of  $U_d^P$ , which indirectly indicated that the initial porosity at this stage was not completely compacted. However, in Figure 13a, stage I corresponded to the initial high in situ stress state recovery stage. Under the comprehensive actions of high effective stresses, the initial micropores in layered sandstones at this stage were three-dimensional compacted, even close to rigid, and the compaction degree was greatly and completely improved. Therefore,  $\eta^P$  at stage I in Figure 13a raised sharply from 0.1634 to 21.51, which indicated that compared with  $U_d^P$ ,  $U_e^P$  at this stage was dominant.

In addition, in Figure 12a, stage ② corresponded to the pre-peak elastic and plastic deformation stage. In this stage,  $\eta^P$  raised sharply from 0.159 to 4.26, which indicated that  $U_e^P$  in this stage was gradually displacing  $U_d^P$ . Finally,  $U_e^P$  was gradually dominant in this stage. It also indirectly indicated that the derivative rate of  $U_d^P$  required for the derivation, development and nucleation of pre-peak nascent cracks and the gradual formation of dominant seepage channels was significantly weaker than the accumulation rate of  $U_e^P$ . Then, it could also verify the rationality of Griffith’s strength theory. However, in Figure 13a, stage II corresponded to the constant axial pressure–unloading confining pressure stage. In this stage,  $\eta^P$  dropped rapidly from 21.51 to 0.55, and the radial openings of micro-cracks opened rapidly. Then, it could provide the adequate spaces for the release of  $U_e^P$  accumulated in stage I, which led to the sharply rising growth rate of  $U_d^P$  at this stage. The dropped characteristic of  $U_e^P$  was significant, and  $U_d^P$  was dominant at this stage.

In addition, in Figure 12a, stage ③ corresponded to the post-peak failure stage. At this stage,  $\eta^P$  dropped rapidly from 4.26 to 0.146 again. Due to the formation of a macroscopic fracture plane, the  $U_e^P$  that was accumulated was rapidly dropped, which led to  $U_d^P$  sharply raising. Compared with  $U_e^P$ ,  $U_d^P$  was dominant at this stage. In Figure 13a, stage III-① corresponded to the pre-peak elastic and plastic deformation stage. Similarly, compared with the  $\eta^P$  of stage ② under CTLTP, the  $\eta^P$  of TLUTP raised rapidly from 0.55 to 5.23 again, and  $U_e^P$  was dominant. However, compared with the  $\eta^P$  of stage ② under CTLTP, the increased amplitude of  $\eta^P$  under TLUTP was gentler, which was the action result of the stage II.

Therefore, it was noted that the peak of  $\eta^P$  at stage III-① was labeled as  $\eta_{\max}^P$ , and the peak of  $\eta^P$  at the end of stage I was “spurious” peak, which was not included in the subsequent analysis. In addition, in Figure 14a, stage III-② corresponded to the post-peak failure stage. Similar to the  $\eta^P$  of CTLTP, the  $\eta^P$  with TLUTP dropped rapidly from 5.23 to 0.21 again in this stage. Compared with  $U_e^P$ ,  $U_d^P$  was dominant in this stage.

In addition, the  $\eta_{\max}^P$  of TLUTP was basically lower than that of CTLTP under identical working conditions (see Figure 14a–c). Among them, the proportion of  $\eta_{\max}^P$  with CTLTP exceeded that with TLUTP, which could reach the highest value of 95.81%. It also indicated that the fracture degree under TLUTP was much weaker than that under CTLTP.

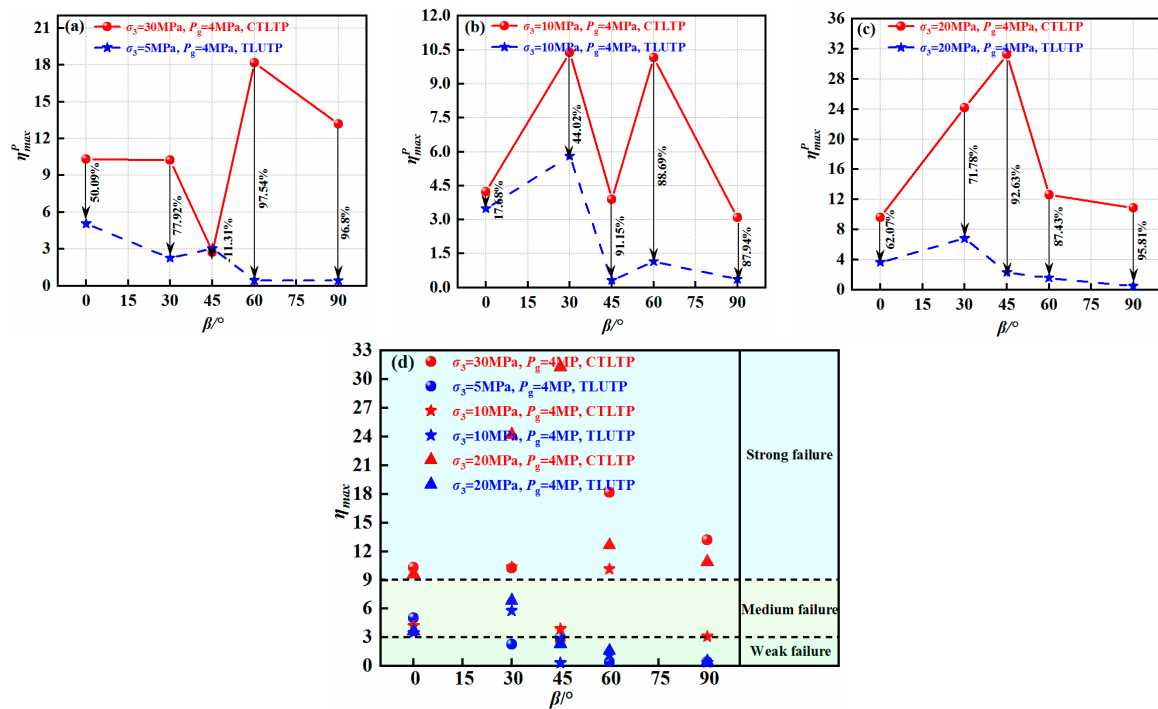


Figure 14. The  $\eta_{max}^P$  and fracture degree.

In addition, as shown in Figure 14d, the criterion for the fracture degree was determined according to the distribution range of  $\eta_{max}^P$ . Among them, when  $\eta_{max}^P \in [0, 3]$ , it was the weak fracture degree; when  $\eta_{max}^P \in (3, 9]$ , it was the medium-strong fracture degree; when  $\eta_{max}^P \in (9, +\infty)$ , it was the strong fracture degree. Therefore, the fracture degree under TLUTP was the weak and medium-strong fracture, and the proportion of the weak fracture degree was higher. However, the fracture degree under CTLTP was the medium and strong fracture, and the proportion of the strong fracture degree was higher.

### 3.5. Energy Anisotropy

In addition, the energy evolution showed significant anisotropy under CTLTP and TLUTP. Therefore, the relationships between  $U_{ecf}^P$ ,  $\sigma_{1cf}^P$  and  $\epsilon_{1cf}^P$  under CTLTP and TLUTP needed to be further clarified (see Figure 15).

As shown in Figure 15a,c,  $U_{ecf}^P$  under CTLTP and TLUTP had a significant linear evolution relationship with the peak stress. However,  $\sigma_{1cf}^P$  was more suitable to estimate the elastic energy storage limit than  $\epsilon_{1cf}^P$ .

The peak elastic energy density under CTLTP and TLUTP showed the “W” shaped evolution characteristic with increasing layered angles (see Figure 16a,c). When the layered angle was  $60^\circ$ ,  $U_{ecf}^P$  was basically the lowest; when the layered angle was  $30^\circ$ ,  $U_{ecf}^P$  was the highest. It was also noted there was the significant energy anisotropy. However, the influence of the stress path on the evolution characteristics of  $U_{ecf}^P$  was significantly weaker than that of layered angles.

Similarly,  $U_{dcf}^P$  under CTLTP and TLUTP showed the “N” type evolution characteristic with increasing layered angles (see Figure 17a,c). When the layered angle was  $90^\circ$ ,  $U_{dcf}^P$  under TLUTP was the highest. When the layered angle was  $60^\circ$ ,  $U_{dcf}^P$  under TLUTP was the lowest.

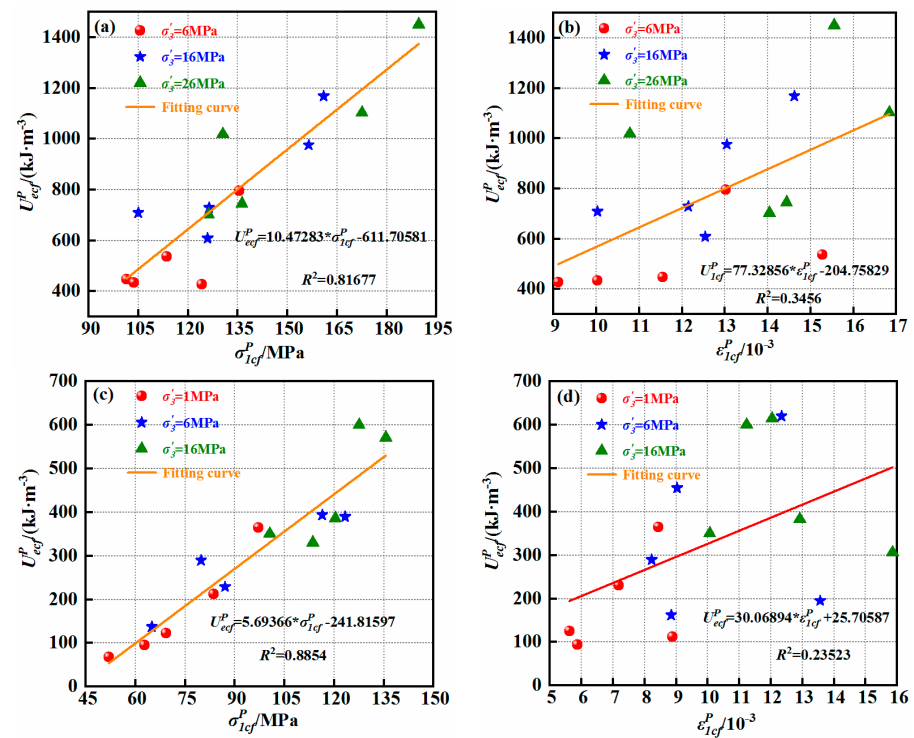


**Figure 15.** The relationships between the peak stress  $\sigma_{1cf}^P$ , peak strain  $\varepsilon_{1cf}^P$  and the peak elastic energy density  $U_{ecf}^P$ : (a)  $\sigma_{1cf}^P$  and  $U_{ecf}^P$  under CTLTP, (b)  $\varepsilon_{1cf}^P$  and  $U_{ecf}^P$  under CTLTP, (c)  $\sigma_{1cf}^P$  and  $U_{ecf}^P$  under TLUTP and (d)  $\varepsilon_{1cf}^P$  and  $U_{ecf}^P$  under CTLTP.

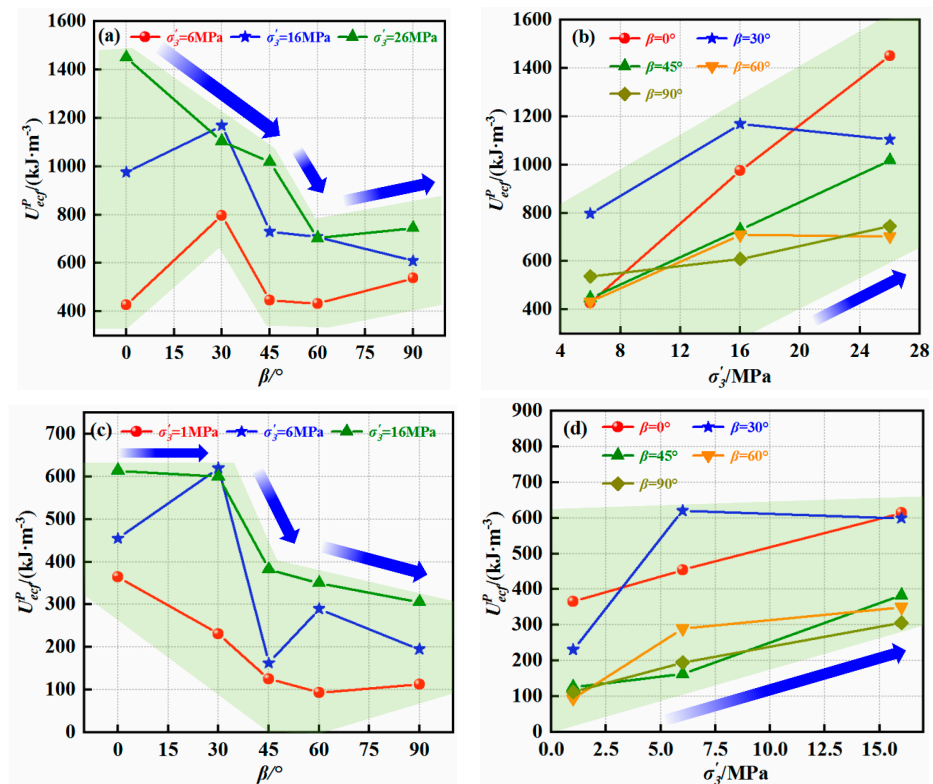


**Figure 16.** Peak elastic energy density: (a) the influences of layered angles under CTLTP, (b) the influences of confining pressure under CTLTP, (c) the influences of layered angles under TLUTP and (d) the influences of confining pressure under TLUTP.

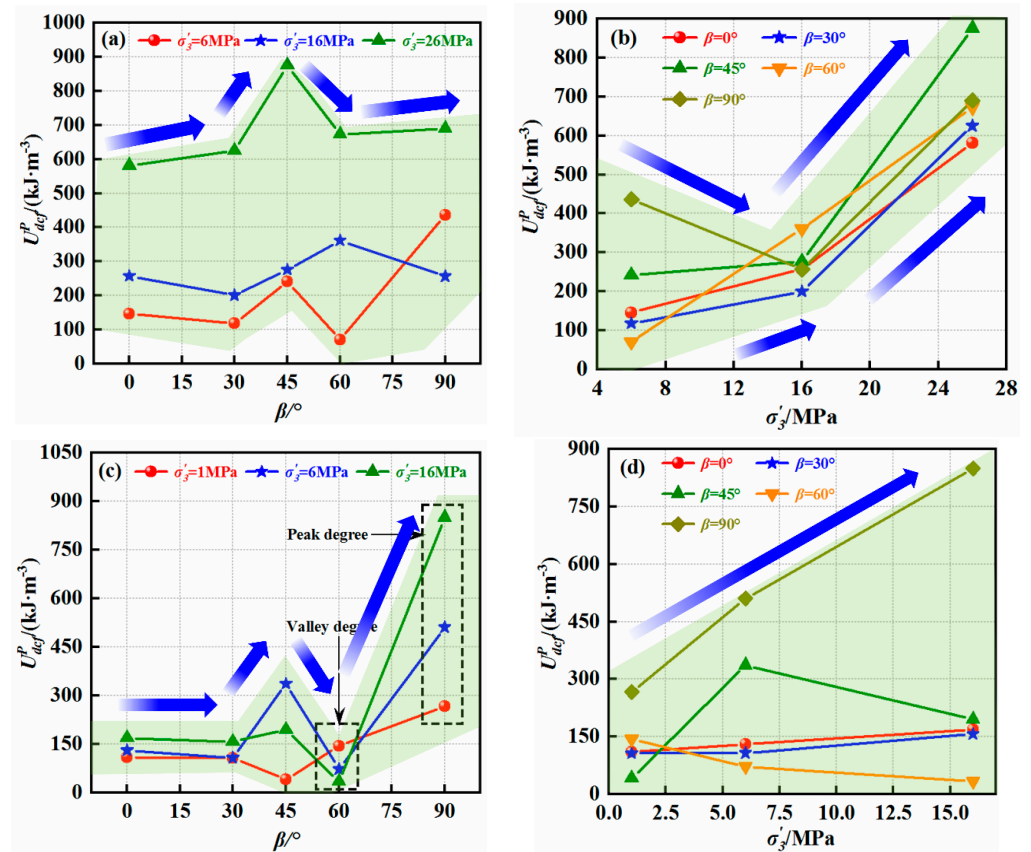


**Figure 17.** Peak dissipated energy density: (a) the influences of layered angles under CTLTP, (b) the influences of confining pressure under CTLTP, (c) the influences of layered angles under TLUTP and (d) the influences of confining pressure under TLUTP.

Similarly,  $U_{tcf}^p$  under CTLTP showed the “W”-shaped evolution characteristic with increasing layered angles (see Figure 18a,c). When the layered angle was  $60^\circ$ ,  $U_{tcf}^p$  under CTLTP was the lowest. When the layered angle was  $0^\circ$  or  $30^\circ$ ,  $U_{tcf}^p$  under CTLTP was the highest. However,  $U_{tcf}^p$  under TLUTP showed the “V” shape evolution characteristic with increasing layered angles. When the layered angle was  $90^\circ$  or  $0^\circ$ ,  $U_{tcf}^p$  under TLUTP was the highest. When the layered angle was  $45^\circ$  or  $60^\circ$ ,  $U_{tcf}^p$  under TLUTP was the lowest.

As the confining pressure increased,  $U_{ecf}^p$ ,  $U_{dcf}^p$  and  $U_{tcf}^p$  under an identical bedding angle all showed a significant increasing trend, but the influence of a stress path was not significant (see Figure 16b,d, Figure 17b,d and Figure 18b,d).

In conclusion, the effects of layered angles, H-M coupling and stress paths could influence the energy anisotropy. However, compared with the influences of H-M coupling and stress paths, the influence of layered angles on energy anisotropy was stronger.

### 3.6. Energy Evolution Model

As shown in Figures 19 and 20, the nonlinear evolution relationships between  $U_{ecf}^p$ ,  $U_{dcf}^p$  and  $U_{tcf}^p$ , effective for confining pressure and layered angles under CTLTP and TLUTP, were obtained. The specific expression of the energy evolution models was as follows:

$$z = z_0 + a\beta + b\sigma_3' + c\beta^2 + d\sigma_3'^2 + e\beta\sigma_3'.$$

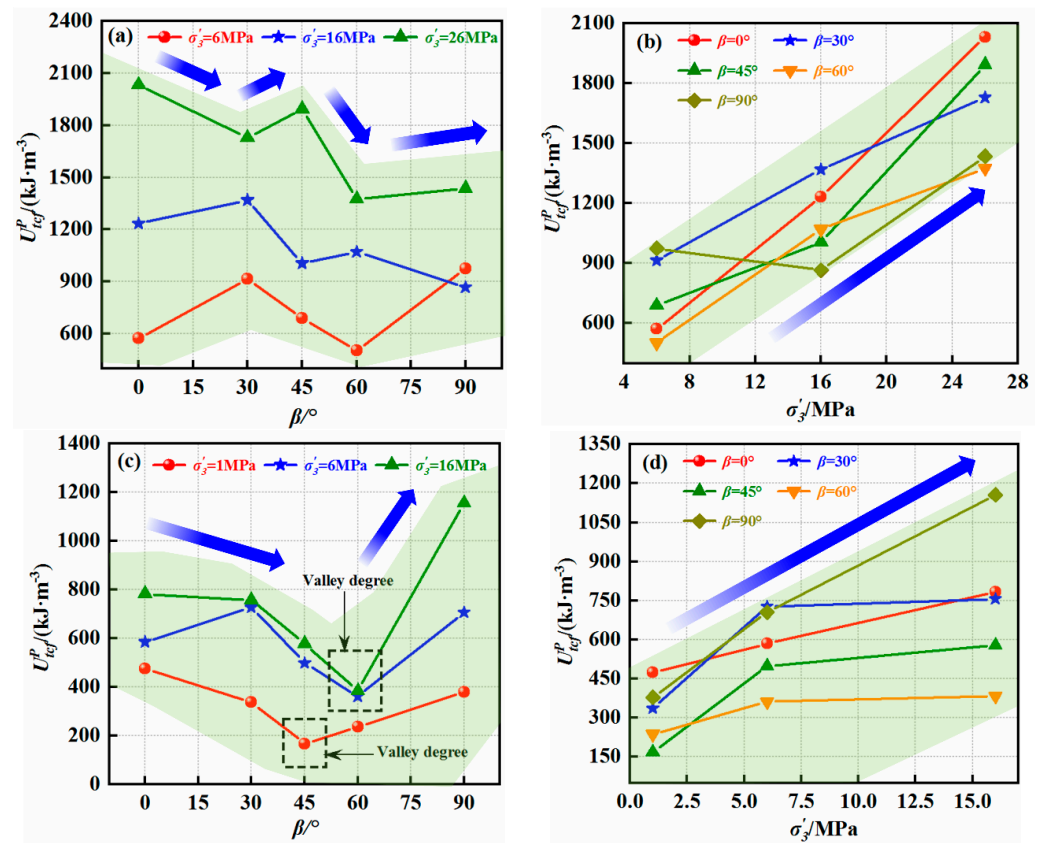


**Figure 18.** Peak total input energy density: (a) the influences of layered angles under CTLTP, (b) the influences of confining pressure under CTLTP, (c) the influences of layered angles under TLUTP and (d) the influences of confining pressure under TLUTP.

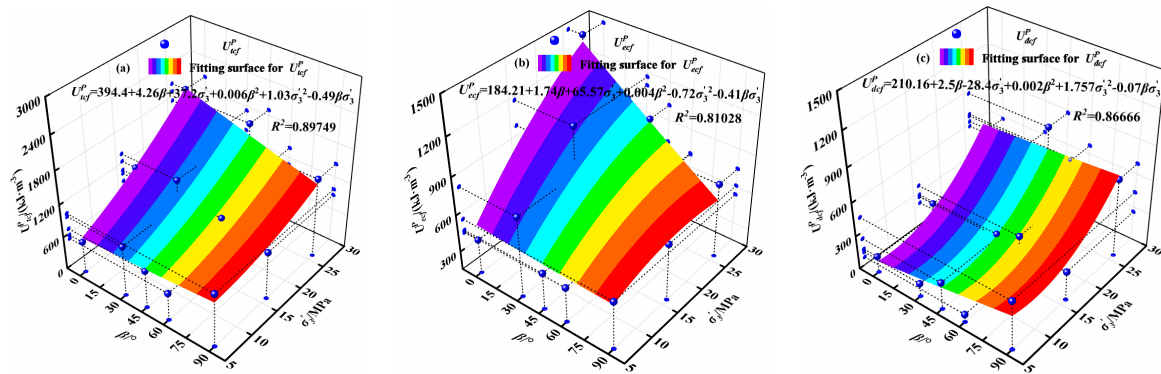


**Figure 19.** Energy evolution models under CTLTP.

Based on the above evolution models, the elastic energy storage capacity under CTLTP and TLUTP could be effectively and accurately estimated, which thus provided more accurate guidance and references for field engineering.

### 3.7. Fracture Mechanism

Combined with Section 3.1, under the combined actions of H-M coupling, layered angles and stress paths, a series of mechanical behaviors occurred on the weakest structure, and finally the main shear fracture with single or crossing cracks was formed. However, according to Griffith's strength theory, the energy was easy to accumulate in the tips of the weakest structure, which could be regarded as the starting source.

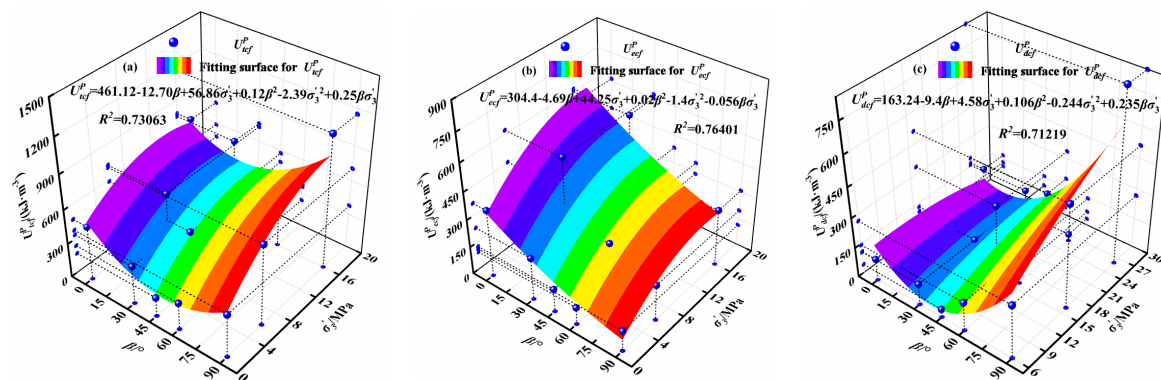


Figure 20. Energy evolution models under TLUTP.

Therefore, as shown in Figure 21, according to the concept of “Energy Flow” and combined with the domino effect [48,52], the energy accumulated in the high-stress concentration zone at the tips of the weakest structure would continuously impact the low-state damage zone, which could be regarded as the target source here. Furthermore, the gradual derivation and expansion of the weakest structure was constantly driven, so that the local damage zone gradually expanded to the main fracture zone [47,48].

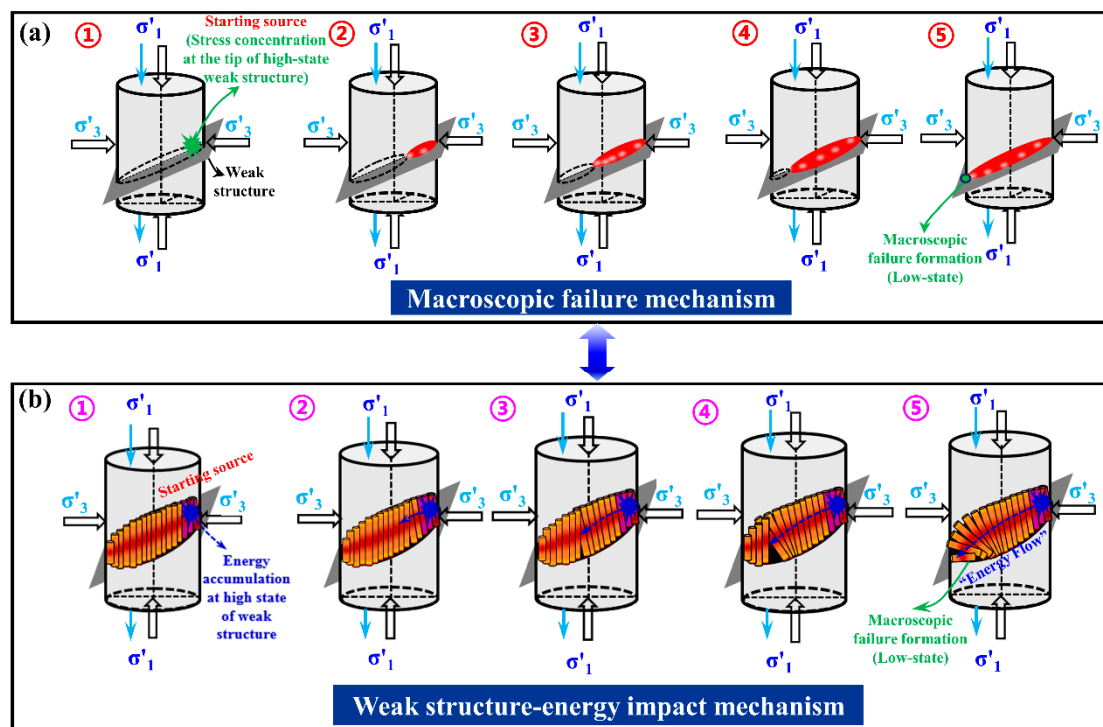


Figure 21. Fracture mechanism: (a) stress perspective, (b) energy perspective (“Energy Flow” perspective) [48].

#### 4. Sublimation and Application of “Energy Flow” Fracture Mechanism

The proposed “Energy Flow” fracture mechanism of layered sandstone was proposed with a laboratory scale. The “Energy Flow” was a directional medium with a definite starting source and target source, thus forming a complete “Energy Flow” chain. Similarly, as shown in Figure 22, the fracture position of the confined water key layer could be regarded as a weak structure to a certain extent, which was one of the starting sources (energy accumulation,  $U_1$ ). Meanwhile, the “Energy Flow” 1 (“Longitudinal Flow”) was generated.

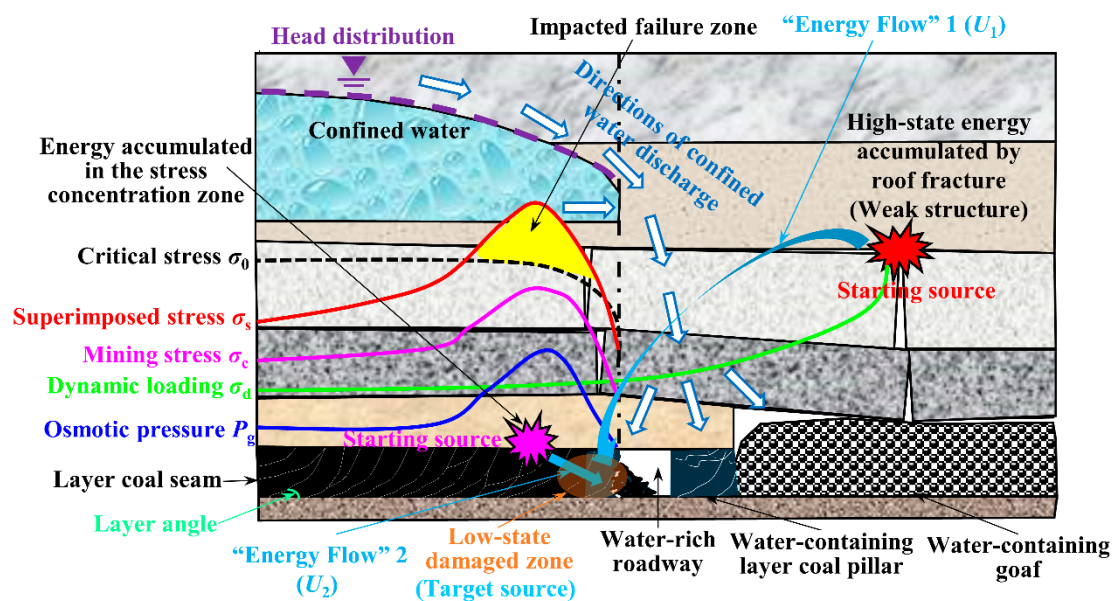


Figure 22. Occurrence mechanism of rock burst in layered water-rich roadway.

The existence of the goaf and the frontage of the layered roadway would lead to the drainage direction of head distribution in the confined water key layer turn to the layered roadway, layered coal pillar and goaf. Then, they both transferred to form the layered water-rich roadway, layered water-containing coal pillar and water-containing goaf, respectively. Under the combined actions of the osmotic pressure  $P_g$ , the dynamic load  $\sigma_d$  and the mining stress  $\sigma_c$ , the significant high-stress concentration zone (energy accumulation,  $U_2$ ) was easily formed in the surrounding rocks of the water-rich layered roadway (target source), which was the second starting source. Meanwhile, “Energy Flow” 2 (“Transverse Flow”) was generated. Under the comprehensive impacts of two “Energy Flow” chains of “Transverse Flow” and “Longitudinal Flow”, the phenomenon of rock burst occurred in a water-rich layered roadway. Among them, the occurrence of a sufficient condition of rock burst in a water-rich layered roadway was as follows:

The combined actions of osmotic pressure  $P_g$ , dynamic load  $\sigma_d$  and mining stress  $\sigma_c$  that led to the superimposed stress  $\sigma_s$  in the surrounding rocks of a layered roadway (target source) was prone to form a significant high-stress concentration zone, which must be higher than the critical stress  $\sigma_0$ . The specific expression of superimposed stress  $\sigma_s$  was as follows:

$$\sigma_s = \sigma_c + \sigma_d + P_g \quad (6)$$

The specific expression of the sufficient condition of rock burst in a water-rich layered roadway was as follows:

$$\sigma_s > \sigma_0 \quad (7)$$

The specific expression of  $U_2$  accumulated by the corresponding “Transverse Flow” was as follows:

$$U_2 = \frac{(\sigma_c + \sigma_d + P_g)^2}{2E} \quad (8)$$

where  $P_g$  was the osmotic pressure,  $\sigma_d$  was the dynamic load,  $\sigma_c$  was the mining stress and  $E$  was the elastic modulus.

Therefore, the specific energy discrimination expression of rock burst in a water-rich layered roadway was as follows:

$$\frac{\partial U_1}{\partial t} + \frac{\partial U_2}{\partial t} > \frac{\partial U_0}{\partial t} \quad (9)$$

Meanwhile, according to the concept of an “Energy Flow” chain [48], the discriminant converted into the form of “Energy Flow” was as follows:

$$\frac{\left[ (\nabla \vec{U}_1)|_{\Delta T} + (\nabla \vec{U}_2)|_{\Delta T} - (\nabla \vec{U}_0)|_{\Delta T} \right]}{\Delta t} \bullet (\vec{e}_X, \vec{e}_Y, \vec{e}_Z) > 0 \quad (10)$$

Namely, at the identical and very short time interval, when the energy gradient tensor of “Longitudinal Flow”  $(\nabla \vec{U}_1)|_{\Delta T}$  and the energy gradient tensor of “Transverse Flow”  $(\nabla \vec{U}_2)|_{\Delta T}$  jointly impacted the layered water-rich roadway directionally, and the sum of them exceeded the critical energy gradient tensor  $(\nabla \vec{U}_0)|_{\Delta T}$  when the rock burst occurred, the phenomenon of rock burst would occur in the layered water-rich roadway, where  $(\vec{e}_X, \vec{e}_Y, \vec{e}_Z)$  was the directional vector of “Energy Flow”.

Therefore, the essential attributes of the prevention and control of rock burst could be summarized from three aspects.

Firstly, controlling the starting source; for example, the protective layer mining technology, cantilever beam top-cutting releasing-energy technology and deep cavitation absorbing-energy technology were used to weaken the starting source. Then, it could greatly reduce the potential of rock burst.

Second, cutting off the propagation path (cutting off the “Energy Flow” chain), such as the hydraulic fracturing (cutting off the “Longitudinal Flow” chain) and large-diameter drilling (cutting off the “Transverse Flow” chain), could also greatly reduce the potential of rock burst.

Finally, protecting the target source (namely, adding one or more safety covers to the target source), such as the grouting modification technology on the surrounding rocks, roadway layout technology under goaf, protective layer mining technology, etc., could better reduce the possibility of rock burst.

In conclusion, “Energy Flow”, as a directional medium, could better reveal the occurrence mechanism of rock burst in a water-rich roadway. No matter the laboratory scale or engineering scale, it could provide a new perspective and concept for the effective prevention and control for rock burst in deep engineering.

## 5. Conclusions

(1) When  $\beta \in (0^\circ, 30^\circ)$  and  $\beta \in (45^\circ, 90^\circ)$ , the influenced sensitivity of layered angles on the peak strength under TLUTP was weaker than that of confining pressure. When  $\beta \in (30^\circ, 45^\circ)$ , the influence of layered angles on the peak strength was more sensitive than that of confining pressure.

(2) The nonlinear evolution relationships between the peak total input energy, peak elastic energy and peak dissipated energy, effective for confining pressure and layered angles under CTLTP and TLUTP, were obtained. Their specific expression was as follows:  $z = z_0 + a\beta + b\sigma'_3 + c\beta^2 + d\sigma'^2_3 + e\beta\sigma'_3$ .

(3) At an identical and very short time interval, when the energy gradient tensor of “Longitudinal Flow”  $(\nabla \vec{U}_1)|_{\Delta T}$  and the energy gradient tensor of “Transverse Flow”  $(\nabla \vec{U}_2)|_{\Delta T}$  jointly impacted the layered water-rich roadway directionally, and the sum of them exceeded the critical energy gradient tensor  $(\nabla \vec{U}_0)|_{\Delta T}$  when the rock burst occurred, the phenomenon of rock burst would occur in the layered water-rich roadway. Namely, the specific discriminant formula with the form of “Energy Flow” of rock burst in a layered water-rich roadway was as follows:

$$\frac{\left[ (\nabla \vec{U}_1)|_{\Delta T} + (\nabla \vec{U}_2)|_{\Delta T} - (\nabla \vec{U}_0)|_{\Delta T} \right]}{\Delta T} \bullet (\vec{e}_X, \vec{e}_Y, \vec{e}_Z) > 0$$

(4) The nature of the effective prevention and accurate control of rock burst was obtained from three aspects, which corresponded to controlling the starting source, cutting off the “Energy Flow” chain (“Transverse Flow” and “Longitudinal Flow”) and protecting the target source.

**Author Contributions:** Z.S.: Conceptualization, Investigation, methodology, software, data curation, writing—original draft and writing—review and editing. J.Z.: Funding acquisition, visualization, supervision. S.W.: Validation. All authors have read and agreed to the published version of the manuscript.

**Funding:** This study was supported by the National Natural Science Foundation of China (grant nos. 52034009, 51974319), the Yue Qi Distinguished Scholar Project (grant no. 2020JCB01), and China University of Mining and Technology (Beijing) Fundamental Research Fund—Top Innovative Talents Cultivation Fund for Doctoral students (BBJ2023001).

**Institutional Review Board Statement:** Not applicable.

**Informed Consent Statement:** Not applicable.

**Data Availability Statement:** The datasets generated or analyzed during the current study are available from the corresponding author upon reasonable request.

**Conflicts of Interest:** The authors declare that they have no conflict of interest.

## Nomenclature

Nomenclature list with all symbols and abbreviations.

$H$	burial depth (m)
$\sigma_x$	minimum horizontal principal stress (MPa)
$\sigma_y$	maximum horizontal principal stress (MPa)
$\sigma_z$	vertical principal stress (MPa)
$\sigma'_x$	minimum horizontal principal stress after pressure relief (MPa)
$\sigma'_y$	maximum horizontal principal stress after pressure relief
$\sigma'_z$	vertical principal stress under superposition of mining-induced stress (MPa)
$P_g$	osmotic pressure (MPa)
$\sigma_1$	axial stress (MPa)
$\sigma_3$	confining pressure (MPa)
$\varepsilon_1$	axial strain (%)
$\varepsilon_3$	radial strain (%)
$\varepsilon_v$	volumetric strain (%)
$t$	time (min)
$\beta$	bedding angle (°)
$\sigma_{1cf}$	peak axial stress (MPa)
$\varepsilon_{1cf}$	peak axial strain (%)
$\varepsilon_{3cf}$	peak radial strain (%)
$\varepsilon_{vcf}$	peak volumetric strain (%)
$U_e^p$	elastic energy density (kJ/m <sup>3</sup> )
$U_d^p$	dissipated energy density (kJ/m <sup>3</sup> )
$U_t^p$	total input energy density (kJ/m <sup>3</sup> )
$\sigma_1^f$	effective axial stress (MPa)
$\sigma_3^f$	effective confining pressure (MPa)
$E$	elastic modulus (GPa)
$\mu$	Poisson's ratio
$\varepsilon_{1t}$	the final data points of axial strain collected by hydraulic coupling tests
$\varepsilon_{3t}$	the final data points of radial strain collected by hydraulic coupling tests
$\eta^p$	the ratio of elastic energy density to dissipated energy density
$\eta_{\max}^p$	maximum value of the ratio of elastic energy density to dissipated energy density
$U_{ecf}^p$	peak elastic energy density (kJ/m <sup>3</sup> )
$U_{dcf}^p$	peak dissipated energy density (kJ/m <sup>3</sup> )
$U_{tcf}^p$	peak total input energy density (kJ/m <sup>3</sup> )

$\sigma_{1cf}^P$	peak strength (MPa)
$\varepsilon_{1cf}^P$	peak axial strain (%)
$U_1$	"Energy Flow" 1
$U_2$	"Energy Flow" 2
$\sigma_d$	dynamic load (MPa)
$\sigma_c$	mining stress (MPa)
$\sigma_s$	superimposed stress (MPa)
$\sigma_0$	critical stress (MPa)
$(\nabla \vec{U}_1)_{\Delta t}$	energy gradient tensor of "Longitudinal Flow"
$(\nabla \vec{U}_2)_{\Delta t}$	energy gradient tensor of "Transverse Flow"
$(\nabla \vec{U}_0)_{\Delta t}$	critical energy gradient tensor
$(\vec{e}_X, \vec{e}_Y, \vec{e}_Z)_{\Delta T}$	directional vector of "Energy Flow"

## References

- Zheng, H.; Cao, S.Q.; Yuan, W.; Jiang, Q.; Li, S.J.; Feng, G.L. A time-dependent hydro-mechanical coupling model of reservoir sandstone during CO<sub>2</sub> geological storage. *Rock Mech. Rock Eng.* **2022**, *55*, 5845–5861. [\[CrossRef\]](#)
- Hamiel, Y.; Lyakhovsky, V.; Agnon, A. Rock dilation, nonlinear deformation, and pore pressure change under shear. *Earth Planet. Sci. Lett.* **2005**, *237*, 577–589. [\[CrossRef\]](#)
- Xiao, Y.X.; Lee, C.F.; Wang, S.J. Assessment of an equivalent porous medium for coupled stress and fluid flow in fractured rock. *Int. J. Rock Mech. Min. Sci.* **1999**, *36*, 871–881. [\[CrossRef\]](#)
- Zhao, H.G.; Liu, C.; Huang, G.; Yu, B.C.; Liu, Y.B.; Song, Z.L. Experimental investigation on rockburst process and failure characteristics in trapezoidal tunnel under different lateral stresses. *Constr. Build. Mater.* **2020**, *259*, 119530. [\[CrossRef\]](#)
- Cai, W.; Dou, L.M.; Si, G.Y.; Hu, Y.W. Fault-induced coal burst mechanism under mining-induced static and dynamic stresses. *Engineering* **2021**, *7*, 687–700. [\[CrossRef\]](#)
- Li, Z.L.; Dou, L.M.; Cai, W.; Wang, G.F.; He, J.; Gong, S.Y.; Ding, Y.L. Investigation and analysis of the rock burst mechanism induced within fault-pillars. *Int. J. Rock Mech. Min. Sci.* **2014**, *70*, 192–200. [\[CrossRef\]](#)
- Song, Z.X.; Zhang, J.W.; Zhang, L.C.; Dong, X.K.; Niu, W.M.; Zhang, Y. The permeability properties of bedded coal and rock: Review and new insights. *Energy Sci. Eng.* **2022**, *10*, 1544–1565. [\[CrossRef\]](#)
- Song, Z.X.; Zhang, J.W.; Zhang, Y.; Dong, X.K.; Wang, S.Y. Characterization and evaluation of brittleness of deep bedded sandstone from the perspective of the whole life-cycle evolution process. *Int. J. Min. Sci. Technol.* **2023**, *33*, 481–502. [\[CrossRef\]](#)
- Song, Z.X.; Zhang, J.W.; Dong, X.K.; Zhang, Y.; Zhang, Y.J.; An, S. Time-dependent behaviors and volumetric recovery phenomenon of sandstone under triaxial loading and unloading. *J. Cent. South Univ.* **2022**, *29*, 4002–4020. [\[CrossRef\]](#)
- Song, Z.X.; Zhang, J.W. Progressive failure mechanical behaviour and response characteristics of sandstone under stress-seepage coupling. *J. Geophys. Eng.* **2021**, *18*, 200–218. [\[CrossRef\]](#)
- Kang, H.P. Temporal scale analysis on coal mining and strata control technologies. *J. Min. Strata Control Eng.* **2021**, *3*, 5–27. [\[CrossRef\]](#)
- Zhang, J.W.; Song, Z.X.; Wang, S.Y. Experimental investigation on permeability and energy evolution characteristics of deep sandstone along a three-stage loading path. *Bull. Eng. Geol. Environ.* **2021**, *80*, 1571–1584. [\[CrossRef\]](#)
- Zhang, J.W.; Song, Z.X.; Wang, S.Y. Mechanical behavior of deep sandstone under high stress-seepage coupling. *J. Cent. South Univ.* **2021**, *28*, 3190–3206. [\[CrossRef\]](#)
- Geng, J.S.; Cao, L.W. Failure analysis of water-bearing sandstone using acoustic emission and energy dissipation. *Eng. Fract. Mech.* **2020**, *231*, 107021. [\[CrossRef\]](#)
- Kou, M.M.; Liu, X.R.; Wang, Z.Q.; Nowruzpour, M. Mechanical properties, failure behaviors and permeability evolutions of fissured rock-like materials under coupled hydro-mechanical unloading. *Eng. Fract. Mech.* **2021**, *254*, 107929. [\[CrossRef\]](#)
- Li, K.S.; Chen, L.X.; Zhao, Z.; Liu, C.X. Experimental investigation on mechanical, acoustic, and fracture behaviors and the energy evolution of sandstone containing non-penetrating horizontal fissures. *Theor. Appl. Fract. Mech.* **2023**, *123*, 103703. [\[CrossRef\]](#)
- Wang, X.R.; Wang, E.Y.; Liu, X.F.; Zhou, X. Failure mechanism of fractured rock and associated acoustic behaviors under different loading rates. *Eng. Fract. Mech.* **2021**, *247*, 107674. [\[CrossRef\]](#)
- Zhang, D.K.; Meng, T.; Taherdangkoo, R.; Feng, G.; Wen, L.; Butscher, C. Evolution trend and weakening mechanism of mode-I fracture characteristics of granite under coupled thermo-hydro-mechanical and thermal treatments. *Eng. Fract. Mech.* **2022**, *275*, 108794. [\[CrossRef\]](#)
- Wang, Y.; Yi, Y.F.; Li, C.H.; Han, J.Q. Anisotropic fracture and energy characteristics of a Tibet marble exposed to multi-level constant-amplitude (MLCA) cyclic loads: A lab-scale testing. *Eng. Fract. Mech.* **2021**, *244*, 107550. [\[CrossRef\]](#)
- Wang, Y.; Hu, Y.Z.; Gao, S.H. Dynamic mechanical behaviors of interbedded marble subjected to multi-level uniaxial compressive cyclic loading conditions: An insight into fracture evolution analysis. *Eng. Fract. Mech.* **2021**, *241*, 107410. [\[CrossRef\]](#)

21. Shi, Z.M.; Li, J.T.; Wang, J. Research on the fracture mode and damage evolution model of sandstone containing pre-existing crack under different stress paths. *Eng. Fract. Mech.* **2022**, *264*, 108299. [\[CrossRef\]](#)
22. Kou, M.M.; Liu, X.R.; Wang, Z.Q.; Tang, S.D. Laboratory investigations on failure, energy and permeability evolution of fissured rock-like materials under seepage pressures. *Eng. Fract. Mech.* **2021**, *247*, 107694. [\[CrossRef\]](#)
23. Huang, L.S.; Li, B.; Wang, B.; Wu, B.; Zhang, J.X. Study on mechanical properties and energy evolution of coal under liquid nitrogen freezing. *Eng. Fract. Mech.* **2023**, *282*, 109158. [\[CrossRef\]](#)
24. Wang, Y.; Li, C.H.; Han, J.Q. On the effect of stress amplitude on fracture and energy evolution of pre-flawed granite under uniaxial increasing-amplitude fatigue loads. *Eng. Fract. Mech.* **2020**, *240*, 107366. [\[CrossRef\]](#)
25. Li, T.T.; Pei, X.J.; Wang, D.P.; Huang, R.Q.; Tang, H. Nonlinear behavior and damage model for fractured rock under cyclic loading based on energy dissipation principle. *Eng. Fract. Mech.* **2019**, *206*, 330–341. [\[CrossRef\]](#)
26. Wang, X.; Su, O.K. Specific energy analysis of rock cutting based on fracture mechanics: A case study using a conical pick on sandstone. *Eng. Fract. Mech.* **2019**, *213*, 197–205. [\[CrossRef\]](#)
27. Gong, F.Q.; Luo, S.; Yan, J.Y. Energy storage and dissipation evolution process and characteristics of marble in three tension-type failure tests. *Rock Mech. Rock Eng.* **2018**, *51*, 3613–3624. [\[CrossRef\]](#)
28. Gong, F.Q.; Yan, J.Y.; Luo, S.; Li, X.B. Investigation on the linear energy storage and dissipation laws of rock materials under uniaxial compression. *Rock Mech. Rock Eng.* **2019**, *52*, 4237–4255. [\[CrossRef\]](#)
29. Gong, F.Q.; Zhang, P.L.; Luo, S.; Li, J.C.; Huang, D. Theoretical damage characterisation and damage evolution process of intact rocks based on linear energy dissipation law under uniaxial compression. *Int. J. Rock Mech. Min. Sci.* **2021**, *146*, 104858. [\[CrossRef\]](#)
30. Luo, S.; Gong, F.Q. Linear energy storage and dissipation laws during rock fracture under three-point flexural loading. *Eng. Fract. Mech.* **2020**, *234*, 107102. [\[CrossRef\]](#)
31. Luo, S.; Gong, F.Q. Energy storage and dissipation laws of rocks under preset angle shear conditions. *Rock Mech. Rock Eng.* **2020**, *53*, 3303–3323. [\[CrossRef\]](#)
32. Gong, F.Q.; Zhang, P.L.; Du, K. A novel staged cyclic damage constitutive model for brittle rock based on linear energy dissipation law: Modelling and validation. *Rock Mech. Rock Eng.* **2022**, *55*, 6249–6262. [\[CrossRef\]](#)
33. Gong, F.Q.; Zhang, P.L.; Xu, L. Damage constitutive model of brittle rock under uniaxial compression based on linear energy dissipation law. *Int. J. Rock Mech. Min. Sci.* **2022**, *160*, 105273. [\[CrossRef\]](#)
34. Liu, X.S.; Ning, J.G.; Tan, Y.L.; Gu, Q.H. Damage constitutive model based on energy dissipation for intact rock subjected to cyclic loading. *Int. J. Rock Mech. Min. Sci.* **2016**, *85*, 27–32. [\[CrossRef\]](#)
35. Hao, T.S.; Liang, W.G. A new improved failure criterion for salt rock based on energy method. *Rock Mech. Rock Eng.* **2016**, *49*, 1721–1731. [\[CrossRef\]](#)
36. Zhang, L.M.; Cong, Y.; Meng, F.Z.; Wang, Z.Q.; Zhang, P.; Gao, S. Energy evolution analysis and failure criteria for rock under different stress paths. *Acta. Geotech.* **2021**, *16*, 569–580. [\[CrossRef\]](#)
37. Razavi, S.M.J.; Aliha, M.R.M.; Berto, F. Application of an average strain energy density criterion to obtain the mixed mode fracture load of granite rock tested with the cracked asymmetric four-point bend specimens. *Theor. Appl. Fract. Mech.* **2017**, *97*, 419–425. [\[CrossRef\]](#)
38. Liu, X.Y.; Xiong, Z.H.; Zhang, H.M. Nonlinear strain energy based (NSEB) criterion for quasi-brittle materials under multiaxial stress states. *Constr. Build. Mater.* **2023**, *375*, 131001. [\[CrossRef\]](#)
39. Mei, J.; Yang, L.; Sheng, X.C.; Ma, X.J.; Sui, B.; Yang, W.M. An experimental and theoretical investigation of time-dependent cracking and creep behavior of rocks under triaxial hydro-mechanical coupling. *Theor. Appl. Fract. Mech.* **2021**, *115*, 103046. [\[CrossRef\]](#)
40. Mei, J.; Sheng, X.C.; Yang, L.; Zhang, Y.L.; Yu, H.H.; Zhang, W.Z. Time-dependent propagation and interaction behavior of adjacent cracks in rock-like material under hydro-mechanical coupling. *Theor. Appl. Fract. Mech.* **2022**, *122*, 103618. [\[CrossRef\]](#)
41. Liu, Q.; Zhao, Y.L.; Tang, L.M.; Liao, J.; Wang, X.G.; Tan, T.; Chang, L.; Luo, S.L.; Wang, M. Mechanical characteristics of single cracked limestone in compression-shear fracture under hydro-mechanical coupling. *Theor. Appl. Fract. Mech.* **2022**, *119*, 103371. [\[CrossRef\]](#)
42. Yan, B.Q.; Kang, H.P.; Li, X.S.; Qi, Q.J.; Zhang, B.; Liu, J.Z. Damage constitutive model and mechanical properties of jointed rock mass under hydro-mechanical coupling. *Theor. Appl. Fract. Mech.* **2023**, *123*, 103735. [\[CrossRef\]](#)
43. Liu, W.; Zheng, L.G.; Zhang, Z.H.; Liu, G.; Wang, Z.L.; Yang, C. A micromechanical hydro-mechanical-damage coupled model for layered rocks considering multi-scale structures. *Int. J. Rock Mech. Min. Sci.* **2021**, *142*, 104715. [\[CrossRef\]](#)
44. Wang, H.L.; Xu, W.Y.; Shao, J.F. Experimental researches on hydro-mechanical properties of altered rock under confining pressures. *Rock Mech. Rock Eng.* **2014**, *47*, 485–493. [\[CrossRef\]](#)
45. Parisio, F.; Vilarrasa, V.; Laloui, L. Hydro-mechanical modeling of tunnel excavation in anisotropic shale with coupled damage-plasticity and micro-dilatant regularization. *Rock Mech. Rock Eng.* **2018**, *51*, 3819–3833. [\[CrossRef\]](#)
46. Yang, J.X.; Mamadou, F.; Guo, G.L. A three-dimensional hydro-mechanical model for simulation of dilatancy controlled gas flow in anisotropic claystone. *Rock Mech. Rock Eng.* **2020**, *53*, 4091–4116. [\[CrossRef\]](#)
47. Song, Z.X.; Zhang, J.W. Research on the progressive failure process and fracture mechanism of rocks with the structural evolution perspective. *J. Struct. Geol.* **2022**, *154*, 104484. [\[CrossRef\]](#)
48. Song, Z.X.; Zhang, J.W.; Wang, S.Y.; Dong, X.K.; Zhang, Y. Energy evolution characteristics and weak structure—“Energy Flow” impact damaged mechanism of deep-bedded sandstone. *Rock Mech. Rock Eng.* **2023**, *56*, 2017–2047. [\[CrossRef\]](#)

49. Li, Y.J.; Li, X.S.; Yin, G.Z.; Yao, J.W. Similar material experimental study on the “domino effect” of the stope pillar unstable failure of gently inclined and medium thick phosphate rock under pillar and room caving. *Disaster Adv.* **2012**, *5*, 77–82.
50. Sisodiya, M.; Zhang, Y.D. A time-dependent directional damage theory for brittle rocks considering the kinetics of microcrack growth. *Rock Mech. Rock Eng.* **2022**, *55*, 2693–2710. [[CrossRef](#)]
51. Chen, Z.X.; Guo, X.X.; Shao, L.T.; Li, S.Q.; Tian, X.J. Design of a three-dimensional earth pressure device and its application in a tailings dam construction simulation experiment. *Acta. Geotech.* **2021**, *16*, 2203–2216. [[CrossRef](#)]
52. Han, L.J.; He, Y.N.; Zhang, H.Q. Study of rock splitting failure based on Griffith strength theory. *Int. J. Rock Mech. Min. Sci.* **2016**, *83*, 116–121. [[CrossRef](#)]

**Disclaimer/Publisher’s Note:** The statements, opinions and data contained in all publications are solely those of the individual author(s) and contributor(s) and not of MDPI and/or the editor(s). MDPI and/or the editor(s) disclaim responsibility for any injury to people or property resulting from any ideas, methods, instructions or products referred to in the content.